

# Assessment of plot scale sediment transport on young moraines in the Swiss Alps using a fluorescent sand tracer

Fabian Maier<sup>a,b\*</sup>, Florian Lustenberger<sup>a,c\*</sup> & Ilja van Meerveld<sup>a</sup>

5 <sup>a</sup> University of Zurich, Dept. of Geography, Winterthurerstrasse 190, CH-8057 Zurich, Switzerland

<sup>b</sup> Nationale Genossenschaft für die Lagerung radioaktiver Abfälle (Nagra), Wettingen, Switzerland

<sup>c</sup> Swiss Federal Institute for Forest, Snow and Landscape Research WSL, Mountain Hydrology and Mass Movements, Zuercherstrasse 111, CH-8903 Birmensdorf, Switzerland

10

\* These authors contributed equally to this work

Corresponding author: Tel.: +41 44 63 55232. E-mail address: fabian.maier@geo.uzh.ch.

July 28, 2023

15 Resubmission of manuscript 2023-899 to Hydrology and Earth System Sciences

**Keywords:** erosion, transport distance, surface runoff, rainfall simulation, photoluminescence, particle tracing

## Abstract

20 Glacial retreat uncovers large bodies of unconsolidated sediment that are prone to erosion. However, our knowledge of over-land flow (OF) generation and sediment transport on moraines that have recently become ice-free is still limited. To investigate how the surface characteristics of young moraines affect OF and sediment transport, we installed five bounded runoff plots on two moraines of different ages in a proglacial area of the Swiss Alps. On each plot we conducted three sprinkling experiments to determine OF characteristics (i.e., total OF, peak OF flow rate) and measured sediment transport (turbidity, sediment concentrations, and total sediment yield). To determine and visualize where sediment transport takes place, we used a fluorescent sand tracer with an afterglow, together with UV and LED lamps and a high-resolution camera. The results highlight the ability of this field setup to detect sand movement, even for individual fluorescent sand particles (300 – 500 µm grain size), and to distinguish between the two main mechanisms of sediment transport: OF-driven erosion and splash erosion. The higher rock cover on the younger moraine resulted in longer sediment transport distances and a higher sediment yield. In contrast, the

25

30 higher vegetation cover on the older moraine promoted infiltration and reduced the length of the sediment transport pathways. The study, thus, demonstrates the potential of the use of fluorescent sand with an afterglow to determine sediment transport pathways, and that these observations can help to improve our understanding of OF and sediment transport processes on complex natural hillslopes.

## 35 **1 Introduction**

Soil erosion rates in alpine regions are high (Panagos et al., 2015; Gianinetto et al., 2020; Musso et al., 2020a) and are expected to increase because of climate change. Rapid glacier retreat exposes unvegetated areas that are prone to surface erosion (Klaar et al., 2015). These changes will affect water quality (Brighenti et al., 2019; Colombo et al., 2019), fish habitats (Carnahan et al., 2019; Cowie et al., 2014), and the longevity of hydropower reservoirs (Li et al., 2022). Climate change is expected to also  
40 increase the frequency, intensity and amount of heavy precipitation (Gobiet and Kotlarski, 2020; Gobiet et al., 2014), which also affects erosion rates and sediment yield (Anache et al., 2018; Maruffi et al., 2022; Nearing et al., 2004). Splash erosion, i.e., the detachment of soil particles by the impact of raindrops, is positively correlated to rainfall intensity (Angulo-Martínez et al., 2012; Fernández-Raga et al., 2017; Park et al., 1983) because the larger raindrops during intense rainfall have a higher kinetic energy (Evans, 1980). If the rainfall intensity is higher than the infiltration capacity of the soil, infiltration-excess  
45 overland flow (i.e., Hortonian Overland Flow, HOF; Horton, 1933) occurs. Saturation-excess overland flow (SOF) occurs during (long) rainfall events that saturate the soil. HOF and SOF can transport the detached particles downslope via interrill erosion, or where flow is concentrated via rill erosion.

Whether OF can transport the detached particles to the bottom of a hillslope or to the stream depends on the connectivity of the source areas to the slope bottom or stream, i.e., whether the two points are connected by water flow (Bracken and Croke,  
50 2007; Smith et al., 2010). This depends on the degree to which transport is facilitated or impeded by surface characteristics and processes. If water infiltrates into the soil after a short distance (i.e., the OF pathways are short), then the OF water and the sediment it carries may not reach the bottom of the hillslope. Sediment connectivity thus depends on the amount of OF and variability in OF, which is affected by the precipitation amount and intensity, the antecedent soil moisture conditions (Nanda et al., 2019), the spatial variability in infiltration rates (Vigiak et al., 2006; Gerke et al., 2015; Cammeraat, 2002), the  
55 microtopography (Appels et al., 2016), and vegetation type and cover (Dunne et al., 1991; Thompson et al., 2010; Wainwright et al., 2000).

The importance of surface hydrological connectivity for sediment yield is well established (see e.g. Bracken et al., 2015; Heckmann et al., 2018; Najafi et al., 2021). Several studies have defined hydrological connectivity (Bracken et al., 2013; Bracken and Croke, 2007) or sediment connectivity indices (Heckmann and Schwanghart, 2013) to quantify the degree to

60 which a system facilitates the transfer of water and sediment (e.g., Asadi et al., 2019; Gay et al., 2016; Heckmann et al., 2018; Lane et al., 2009; Shore et al., 2013; Zanandrea et al., 2021). Connectivity has also been implemented in different conceptual frameworks (Brardinoni and Hassan, 2006; Stock and Dietrich, 2003; Bracken et al., 2013; Bracken and Croke, 2007; Reaney et al., 2014), and has been explored in model studies (Appels et al., 2011; Reaney et al., 2014; Masselink et al., 2017; Peñuela et al., 2016). Much less is known about the real-world connection of OF pathways (Wolstenholme et al., 2020) and how this  
65 affects sediment transport because it is difficult to observe OF pathways and sediment transport during rainfall events. This is particularly the case for vegetated hillslopes, but some studies managed to do so by mapping sediment and flow paths after events (Marchamalo et al., 2016), or by mapping erosion and deposition forms (Calsamiglia et al., 2020).

Connectivity of OF has been studied in arid areas (Smith et al., 2010; Moreno-De Las Heras et al., 2010; Lázaro et al., 2015), agricultural areas (Peñuela et al., 2016; Sen et al., 2010; Buda et al., 2009), and on frozen soils (Coles and McDonnell, 2018).  
70 Dyes and cameras (Polyakov et al., 2021; Wolstenholme et al., 2020; Smith et al., 2010; Gerke et al., 2015) and thermal imaging of heated water (Lima et al., 2015) have been used in rainfall simulation studies on laboratory flumes and in arid areas. For example, Wolstenholme et al. (2020) used visual observations of the OF pathways and highlighted the importance of infiltration along the flowpath and flow resistance for the establishment of connectivity. They also stressed the importance of vegetation, slope, surface stone cover, and surface roughness for OF generation in dryland areas. Marchamalo et al. (2016)  
75 used repeated field mapping in semi-arid catchments to determine the connectivity between sediment source areas and sediment sinks. Calsamiglia et al. (2020) used unmanned aerial vehicles (UAV) and field mapping to, similarly, study the evolution of surface flow pathways and the erosion and deposition of sediments after storm events in a small agricultural catchment. Other studies used radio frequency identification tags (Parsons et al., 2014), diffuse reflectance spectrometry (Martínez-Carreras et al., 2010), and rare earth element tracers (Polyakov and Nearing, 2004; Deasy and Quinton, 2010) to study sediment transport  
80 and connectivity. For example, Guzmán et al. (2015, 2010) used silt-sized magnetite, hematite, magnetic iron oxide, and goethite particle tracers mixed to soil aggregates to study sediment movement on agricultural fields. The tracer and sediment concentrations were measured in the runoff at the bottom of the plots, but no observations were made on the plot surface to determine the actual flow pathways. Tauro et al. (2012b) used buoyant fluorescent polyethylene spheres to determine particle transport velocities on semi-natural hillslopes. They showed that Full HD videos were best for real-time detection of the move-  
85 ment of these rather large spheres (1.0 – 1.2 mm). However, their fluorescent spheres did not have the same shape as natural soil particles and a different buoyancy (i.e., the particles could float on the water). Sand particles coated with a fluorescent paint represent the size and density of natural soil particles more closely than fluorescent spheres and have been used to track sediment movement on beaches (Ingle, 1966), along the surf zone in the Nile river delta (Badr and Lotfy, 1999), to study on- and offshore sediment transport along the coast of Israel (Klein et al., 2007), and sand movement in a river tidal flat in Japan  
90 (Kato et al., 2014). Hardy et al. (2017 and 2019) used a fluorescent sand tracer with a similar particle size and density as the soil to study soil redistribution by tillage on arable farmland. Although pioneering studies using fluorescent sand (Yasso, 1966)

and glass particles (Young and Holt, 1968) considered it suitable for sediment transport studies more than five decades ago, they have so far not been used to determine rates of sediment movement on natural hillslopes (Parsons, 2019).

We, therefore, tested the use of a fluorescent sand tracer in combination with sprinkling experiments to study sediment transport on two young moraines in the Swiss Alps. The moraines differed in age (one had only been ice-free for three decades and the other for more than a century and half) and therefore surface characteristics (e.g., vegetation cover, rock cover, surface roughness, aggregate stability, and saturated hydraulic conductivity). More specifically, we assessed the following research questions:

- Can fluorescent sand particles be used to trace sediment transport on young moraines?
- Do the derived differences in sediment transport distances explain the differences in sediment concentrations and sediment yield at the bottom of the plot?
- How are sediment yield and sediment transport distances related to the surface characteristics (slope, vegetation cover, surface roughness, soil aggregate stability, and saturated hydraulic conductivity)?

We hypothesized that higher rainfall intensities lead to more OF and sediment transport (Medeiros and de Araújo, 2013; Buendia et al., 2016; van De Giesen et al., 2000) and that there would be more OF on the older moraine due to the lower infiltration rates into the finer matrix (Lohse and Dietrich, 2005; Maier et al., 2020). However, we expected that sediment transport distances would be shorter and erosion rates would be lower for the older moraine due to the higher vegetation cover (Geißler et al., 2012; Greinwald et al., 2021a). We, furthermore, expected that the higher surface roughness and larger depression storage for the younger moraine, together with the higher effective infiltration rates in these depressions, would lead to a decrease in connectivity and sediment yield (cf. Govers et al., 2000).

## 2 Site description

### 2.1 Study area

The field measurements were conducted between August and September 2018 in the forefield of the Steigletscher, south of the Sustenpass mountain road in the Central Swiss Alps (46°43' N, 8°25' E; Figure 1). The elevation of the glacial forefield ranges between 2000 and 2100 m above sea level (m a.s.l.). The study area is part of the internal alpine massif (Aarmassif) and underlain by the highly polymetamorphic “Erstfelder”-gneiss-zone. It predominantly contains biotite-plagioclase-gneiss, pre-mesozoic metagranitoids and amphibolites (Labhart, 1977).

The mean annual air temperature (1991 – 2020) at the closest long-term automatic weather station (the Grimsel Hospiz, located 20 km from the study area at 1980 m a.s.l.) is 2.3 °C (MeteoSwiss, 2022). The average monthly temperature for the same period varies between -4.9 °C in February and 10.3 °C in August. The mean annual precipitation at the Grimsel Hospiz is 1834

mm y<sup>-1</sup>, and is evenly distributed over the year. Snowfall events are frequent, even during the summer months. On average, there is more than 10 cm of snow on the ground for 210 days per year (MeteoSwiss, 2022). Even though streamflow is dominated by snow and glacier melt, high-intensity rainfall events are also important. The 30-minute rainfall intensity with a 10-year return period is 36 mm h<sup>-1</sup> (95 % confidence interval: 30 – 46 mm h<sup>-1</sup> (1990 – 2020 period; MeteoSwiss, 2021)).

Based on glacier extend maps for the last 150 years and aerial images (Swiss Federal Office of Topography – 'Journey through time' – Map and 'SWISSIMAGE Journey through time' – Aerial Images), we selected two moraines that could be dated precisely (Figure 1). The older moraine originates from the little ice age (hereafter called 1860 moraine), while the younger moraine became ice-free only in 1990 (hereafter referred to as the 1990 moraine; c.f. Musso et al., 2020b; Maier and van Meerveld, 2021). Both moraines were located ~900 m north from the terminus of the Steigletscher in 2018. The 1990 moraine is located ~30 m higher than the 1860 moraine. Both moraines are side moraines and are northeast-exposed.

The 1860 moraine is largely covered by alpine sweet vernalgrass (*Anthoxanthum alpinum*), bellflowers (*Campanula scheuchzeri*), pale clover (*Trifolium pallescens*) and willow (*Salix retusa* and *Salix glaucoserica*; Table 1). The 1990 moraine is dominated by fields of scree (Table 1) and pioneer plant species, such as pale clover (*Trifolium pallescens*), alpine bluegrass (*Poa alpina*) and alpine willowherb (*Epilobium fleischeri*; Table 1). Typical early-successional communities on coarse-textured soils, such as *Salix retusa* and *Salix hastata* with shallow root systems (Hudek et al., 2017; Jonasson and Callaghan, 1992; Lichtenegger, 1996; Pohl et al., 2011) can be found on the 1990 moraine as well. Vegetation cover, root density and organic matter content are higher for the 1860 moraine than the 1990 moraine (Greinwald et al., 2021b).

The soils of both moraines are sandy-loamy Hyperskeletal Leptosols, are very young and contain coarse gravel fragments, sand and buried stones throughout the profile (Musso et al., 2019). The soil texture in the upper 50 cm of soil is similar for the two moraines, with sand (particle diameter 63 µm – 2 mm) being the dominant texture (~75 %; Hartmann et al., 2020a).

## 2.2 Study plots

On each moraine, we installed three 4 m by 6 m bounded runoff plots (Figure 1 & Table 1). To cover as much variability as possible on each moraine, we chose the location of the plots based on vegetation cover and functional diversity (Garnier et al., 2016; Maier et al., 2020; Greinwald et al., 2021b). More specifically, we selected the area with the lowest (L), intermediate (M) and highest (H) vegetation complexity on each moraine (Table 1; Maier and van Meerveld, 2021). Vegetation complexity is an index based on the vegetation cover, number of different species, and functional diversity (based on stem growth form, root type, clonal growth organ, seed mass, Raunkiaer's life form, leaf dry matter content, nitrogen content, and specific leaf area (Garnier et al., 2016; Greinwald et al., 2021b)). The vegetation cover was 80, 80 and 95 % for the L, M and H plots on the 1860 moraine and 50, 30 and 45 % for the L, M and H plots on the 1990 moraine, respectively (Table 1, Figure 1). Because the 1860H plot was covered with dense shrubs of alpine rose that obscured the fluorescent sand, this plot was not included in

any of the analysis (i.e., we report the results for five plots only). The plots were all steep, with the average slope varying between 21° and 36° (Table 1). However, the topographic position of the plots differed. The 1860L, 1860M and 1990M plots were located at a mid-slope position, while the 1990L and 1990H plots were located at the bottom of the slope.

### 3 Methods

#### 3.1 Plot characteristics

##### 3.1.1 Surface topography and rock cover

The slope angle for the plots was determined based on twelve measurements with an inclinometer (every 50 cm at both sides of each plot). We report the average value for the seven measurements on the bottom half of the plots where the fluorescent sand and blue dye were applied (see Table 1). We chose to use the inclinometer slope over the slope derived from the DSM (see section 3.4) because of the somewhat coarse resolution of the DSM and the distortion by the vegetation cover. However, the correlation between the mean slope derived from the DSM and the inclinometer measurements was high ( $r = 0.94$ ) and the difference was less than 3° for all plots.

A 1.5 m long microtopography profiler, consisting of a wooden frame with 101 adjustable 1 m long metal rods (cf. Leatherman, 1987), was used on ten transects within each plot to determine the surface roughness based on the normalized line length and the tortuosity index (cf. Bertuzzi et al., 1990). We report the average values for the six transects on the bottom half of the plots (see Table 1).

Georeferenced and orthorectified photographs from a drone (DJI Phantom 4 Pro; see Figure 1) were used for visualization of the plots and to determine the rock cover based on a supervised classification in Adobe Photoshop CS6 (v13.0.1; tool: “color range”) that is frequently used for digital image analysis (e.g., Dorador et al., 2014; Zhang et al., 2014). After the plot area was selected with the “marquee” tool, the color range tool (selection preview set to “black matte”) was used to determine the color range of stones and rocks. An automatic algorithm adds pixels that correspond to the color range of the test areas to the selection. The selected pixels (i.e., rocks) were visually compared to the drone image and additional test areas were added until all rocks were selected. Then, the number of selected pixels (determined from the histogram) was divided by the total number of pixels of the plot area to obtain the percentage of rock cover.

##### 3.1.2 Soil aggregate stability

We determined the soil aggregate stability for six soil samples taken from the upper 10 cm of soil at each plot using a Humax-Tube® (GreenGround AG) using the method of Bast et al. (2015). In this method, the soil sample is placed on a 20 mm sieve and submerged in water for 5 min. The aggregate stability coefficient (ASC) varies between 0 for complete destruction of the

soil sample to 1 for a fully stable soil sample (Bast et al., 2015). We reported the median ASC-value for each plot (see Greinwald et al., 2021a for more information).

### 3.1.3 Saturated hydraulic conductivity

185 Infiltration rates were measured at three locations next to each plot using a Double-Ring-Infiltrometer (inner diameter of 20 cm; ASTM D3385-03 standard test method). The infiltrometers were inserted vertically into the ground for at least 5 cm on all sides. The ponding depth was 15 – 25 cm. The saturated hydraulic conductivity ( $K_{sat}$ ) was determined based on the steady-state infiltration rate (see also Maier et al., 2020; Maier and van Meerveld, 2021). We report the average value of the three measurements per plot. We acknowledge that many more measurements would be needed to obtain a robust average  $K_{sat}$  value  
190 (e.g., Harden and Scruggs, 2003; Zimmermann, 2008) but due to time limitations more measurements were not possible. Nonetheless, the six (1860 moraine) and nine (1990 moraine) measurements at each moraine already provide some information on the magnitude and variability in  $K_{sat}$ .

## 3.2 Rainfall and overland flow measurements

### 195 3.2.1 Plot set-up

At the left, right and upslope borders of each plot, we inserted plastic sheets approximately 5 cm into the ground to minimize lateral in- and outflow of OF from the plots (Figure 2a). At the downslope border of each plot, we dug a trench and inserted pond foil ~2 – 5 cm into the soil (Figure 2b). The foil was attached to a gutter, which was covered with plastic sheeting to protect it from the rain (Figure 2a). From the gutter, water flowed through a 5 cm diameter hose into an Upwelling Bernoulli  
200 Tube (Stewart et al., 2015), in which a pressure transducer was located (DCX-22-CTD, Keller). At each moraine, another pressure transducer measured the local barometric pressure. From these measurements, the OF rate could be determined at a 1 min interval. Because the pond foil was inserted several centimeters (up to 10 cm) below the soil surface, the measurements of OF also contain biomat flow (cf. Sidle et al., 2007) and very shallow subsurface flow (Figure 2b). However, we refer to this as OF throughout the remainder of this manuscript. For a more detailed description of the OF measurements, see Maier and  
205 van Meerveld (2021).

### 3.2.2 Sprinkling experiments

On each plot, we performed three sprinkling experiments of different intensities over a three-day time period (Table 2). We refer to these three events as low intensity (LI), medium intensity (MI) and high intensity (HI) experiments. We started the rainfall simulations with the low intensity (LI) experiment, did the mid intensity (MI) experiments the next day and the high  
210 intensity (HI) experiments on the third day. We chose this order to minimize the effect of erosion (and deposition) during the first experiment(s) on sediment transport during the later experiments. In case rainfall was expected in the 24 hours before the

LI experiment or between the experiments, the plots were covered with big tarps. As soil moisture measurements at 5 and 15 cm below the soil surface suggested that the topsoil drains to field capacity within a day and subsurface flow generally stopped within two hours after rainfall events (Maier et al., 2021), we did the consecutive experiments on each plot one day after each other, so that soil moisture was at approximately field capacity for the MI and HI experiments.

We used either one, two or three Senninger I-Wob adjustable sprinklers (nozzle number 22) to obtain the different intensities (Figure 2a). The sprinklers were placed at the center line of the plots at 2 m height (Figure 2a). The water was obtained from the nearby glacial stream and stored in two 4 m<sup>3</sup> water reservoirs, located more than 20 m above the plots to ensure sufficient pressure for the sprinklers. From the reservoirs, water flowed through fire hoses, a water meter, and garden hoses to the sprinklers. The area to which rainfall was applied by the sprinklers extended the plot dimensions by at least 0.5 m upslope, approximately 4 m to the left and right of the plots (and several meters downslope). For each experiment, rainfall was applied until total infiltration exceeded 20 mm. The infiltration was determined by subtracting the OF from the applied rainfall. The average sprinkling durations were 68±8 min (LI), 45±9 min (MI) and 39±4 min (HI).

We measured the actual rainfall intensities on the plots using two tipping buckets (Figure 2a) and at the plot boundaries using four manual rain gauges. The actual rainfall intensities for the LI, MI and HI experiments varied (Table 2) because of wind drift and differences in the water pressure. The average sprinkling intensities (± standard deviation) were 19±4 mm h<sup>-1</sup> (LI), 45±10 mm h<sup>-1</sup> (MI) and 65±20 mm h<sup>-1</sup> (HI). The mean coefficient of variation of the measured rainfall was 28±15 % (range: 9 – 48 %).

The median drop size at a rainfall intensity of 39 mm h<sup>-1</sup>, determined using the oil method of Eigel and Moore (1983), was 1.2±0.4 mm (range: 0.4 – 2.7 mm). This drop size is very similar to the value for natural precipitation in mountain regions in Western Europe (~1.1 mm; Hachani et al., 2017) and representative for orographic precipitation (median drop size of 0.1 – 1.5 mm; Blanchard, 1953). We, hence, assumed that the kinetic energy of our rainfall simulation was comparable to that of natural rainfall in the Swiss Alps.

### 3.2.3 Suspended sediment measurements

To determine the sediment concentrations in OF, 500 ml samples were taken from the outflow of the Upwelling Bernoulli Tubes. We started sampling as soon as there was some outflow and continued after the experiment ended until the outflow stopped. More samples were taken on the rising limb than on the falling limb. To determine the amount of sediment per sample, we filtered the samples using 1.6 µm filters (GF/A Whatman), and then dried and weighted the filters. For a more detailed description, see Maier and van Meerveld (2021).

A Cyclops 7 turbidity probe (Turner designs) was installed between the gutter and the Bernoulli Tube (Figure 2a) and measured the turbidity of OF every minute. The turbidity at the time of sampling was related to the sediment concentrations to obtain a moraine specific relation between turbidity and the suspended sediment concentration. The coefficient of determination (R<sup>2</sup>)



for this relation was 0.80 for the 1860 moraine and 0.89 for the 1990 moraine. The regression slope was  $3.1 \text{ mg L}^{-1} \text{ NTU}^{-1}$  for the 1860 moraine and  $3.3 \text{ mg L}^{-1} \text{ NTU}^{-1}$  for the 1990 moraine. These values are comparable to those reported for alpine streams (Paschmann et al., 2017; Geilhausen et al., 2013; Orwin et al., 2010). We used these correlations to obtain time series of the estimated suspended sediment concentration from the turbidity measurements. Finally, the suspended sediment yield was determined for each event based on the sum of the product of the OF rates and the estimated suspended sediment concentrations (see also Maier and van Meerveld, 2021). On the 1990 moraine, some sediment was trapped in the Bernoulli tubes and not sampled. Thus, the sediment yield is slightly higher than estimated this way (estimated error: 1-5% of the total sediment flux per experiment).

### 3.3 Fluorescent sand transport

To determine where sediment transport occurs and how far individual soil particles are transported along a hillslope during a single rainfall event, we applied ribbons of fluorescent sand to the plots and photographed the plots before and after the sprinkling events. The advantage of the use of fluorescent sand over fluorescent spheres is that the particles have the same size, shape and density as the material on the moraines, and that the sand is a lot cheaper.

#### 3.3.1 Field set-up

The night before each sprinkling experiment (10 to 18 hours prior to the experiments), a line of fluorescent sand (Noxton<sup>TM</sup>; Glow in the Dark Sand) was applied to the soil surface in the middle or lower half of the plot (Figure 2c). We chose to apply the sand to the lower half of the plots because OF is more likely to occur there due to the larger contributing area than further upslope. The fluorescent sand was placed in ribbons across the surface of the plot using a plastic tube that was cut in half. The tube was filled with the fluorescent sand, placed carefully on the plot, and then slowly turned to release the sand. The sand, thus, covered not only the soil and rocks but also small patches of short vegetation (see Figure 2 and Figure 8). The applied sand ribbons were about 3 to 5 cm wide and 2 cm thick. They were 1.5 m long on the 1860 moraine and 3.1 m long on the 1990 moraine. The quartz sand is coated with a non-toxic, photoluminescent (fluorescent and phosphorescent), non-dissolvable powder (TAT33), containing  $\text{CaAl}_2\text{O}_4$  and  $\text{Al}_2\text{O}_3$  (Noxton Technologies, 2022). After illumination, the sand has an afterglow for several minutes. The particle size of 300 – 500  $\mu\text{m}$  corresponds well with the grain size on the moraines (median sand (63  $\mu\text{m}$ - 2 mm) content: 82 and 76 % for the top 10 cm of the soil on the 1860 and 1990 moraines, respectively (Hartmann et al., 2020b; Musso et al., 2019)). Because the particles have the same density of sand, they are not very susceptible to wind erosion. We used three different colors of fluorescent sand (orange for the LI, green for the MI, and blue for the HI experiments).

#### 3.3.2 Photographs

Pictures of the fluorescent sand were taken the night before and after each sprinkling experiment. A red-white 0.5 m segmented fluorescent plastic chain (Novap) was installed around the bottom half of the plot and served as a reference marker during the

image analysis later. In addition, thin red fluorescent ropes were placed every 0.5 m across the plot (Figure 2a, c) and served  
275 as approximate distance markers. In the nights before and after the sprinkling experiments, the fluorescent chain, ropes and  
sand were illuminated with six 18W UV lamps (Eurolight) for ~10 min before and while taking photographs. These lamps  
emit light in the ultraviolet (UV) range at around 365 nm. Four lamps were mounted on a pole that was installed over the plot  
(Figure 2c) and two were handheld and moved around the plot to illuminate areas in the shadows of rocks or plants. In the ~10  
min before the photographs were taken, the sand was additionally illuminated with two 23W LED lights to activate the sands  
280 afterglow. The LED lights were moved to different positions around the plots to illuminate the areas in shadows as well.

A camera (Sony Alpha 7R II) with a wide-angle lens (Sony Vario-Tessar® T\* FE 16 – 35 mm F4 ZA OSS) was mounted on  
a tilting angle (to account for the average slope of the plots) on a 4 m high tower below each plot (Figure 2a). This camera was  
used to take photos of the sand ribbons during UV illumination (after LED illumination). The 42-megapixel resolution of the  
photos ( $7952 \times 5304$  pixels) was very good (on the plot surface 1 pixel corresponds to a length of about 0.5 – 0.7 mm), which  
285 allowed for the detection of individual fluorescent sand particles. The photos were saved with full pixel resolution in the RAW-  
format (.ARW file) to obtain a high-quality image with maximum dynamic range, as well as in the JPEG-format for faster  
post-processing. The aperture was set fully open (F/4). During windy nights, the camera tower moved slightly, which led to  
blurry photos when slow shutter speeds were chosen. Thus, during windy conditions, the shutter speed was set to one second  
and high ISO values (up to 8000) were used. During nights with little wind, the shutter speed was set to two, five or ten seconds  
290 to reduce the ISO to 1000 – 5000 (depending on the light conditions) to obtain better quality pictures.

On the 1990L plot, we additionally used a liquid brilliant blue dye tracer during the MI and HI experiments to visualize the  
water flow pathways. We manually added the blue dye tracer to the surface at places where OF was visible. The flow paths of  
the dye tracer were recorded on video in Ultra HD resolution ( $3840 \times 2160$  pixels) with 25 frames per second using the camera  
(Sony Alpha 7R II) on the camera tower. The combination of several video frames led to a composite picture of the flow paths  
295 on the surface, which could then be compared to the movement of the fluorescent sand.

### 3.3.3 Image pre-processing

The photos of the sand ribbons were post-processed to obtain a matrix for each photo, where each element corresponds to one  
pixel with an area of  $1 \text{ mm}^2$  on the plot (cf. Schneider et al., 2014; Weiler, 2001; Weiler and Flühler, 2004), and has a value  
of one if there was fluorescent sand and zero if there was no sand. These matrices are called *classified images* in the remainder  
300 of the text (Figure 3b). The procedure used to classify the images is similar to the supervised classification algorithm (maxi-  
mum likelihood) that is used in remote sensing analyses (e.g., Richards, 2013).

The segmented chain around the plot was used to determine the location of four points of the chain on the photo (top left  
corner, top right corner, a point on the bottom left, and a point of the bottom right of the photos). The color of the chain changes  
every 0.5 m, which facilitated the selection of these points. Known coordinates (measured distances between these points in

305 the field) were assigned to these points. For the resampling, the *skimage.transform.resize* function in Python (v3.8.8) was used within the Scientific Python Development Environment (Spyder v4.1.5). This function uses a Gaussian filter (Gaussian smoothing) to obtain a lower resolution image from a higher resolution image, while avoiding aliasing artefacts. This “geometric correction” was done for all photos. The areas outside the plots were cropped with Adobe Photoshop CC 2021 (v22.2; Figure 3a).

310 The detection of the sand particles was done in the hue, saturation, value (hsv) color space, which has the advantage that a single number (hue) represents the color. If the hue of a pixel was in the specified range for the sand and the value (v) was above 10%, the pixel was classified as fluorescent sand. We chose at least ten representative locations of the sand ribbon on each photo to determine the typical hue of the sand in Adobe Photoshop (orange:  $0^\circ - 80^\circ$  and  $320^\circ - 360^\circ$ , green:  $150^\circ - 180^\circ$ , blue:  $180^\circ - 240^\circ$ ). As the sand had a certain brightness (due to its afterglow), a value (v) of at least 10 % was chosen to  
315 reduce misclassifications in the dark parts (e.g., due to reflections on rocks, vegetation etc.). The classification was done in Python, based on an existing script to detect a brilliant blue dye tracer in soil profiles (Weiler, 2001). To detect the orange sand, the segmented chain and the fluorescent ropes had to be manually removed in Adobe Photoshop because their hue was in the range of the sand. To detect the blue sand, the green sand had to be manually removed in Adobe Photoshop because some green sand particles had a hue within the typical blue sand range (green:  $150^\circ - 190^\circ$ , blue:  $180^\circ - 240^\circ$ ).

#### 320 **3.3.4 Image analysis**

The fluorescent segmented chain around the plot led to tie areas instead of tie points. Furthermore, they became slightly bent during the experiments (due to their weight). As a result, the reference points for the geometric correction differ for the pre- and post-experiment classified images (i.e., the matrix coordinates (0, 0) in the pre- and post-experiment classified images do not have the exact same position on the plot). This means that the pre- and post-classified images cannot be overlain and  
325 subtracted from each other to obtain the change in fluorescent sand covered area. Therefore, a theoretical starting line at approximately the middle of the sand ribbon was defined for all classified images (pre- and post-experiment, cf. Figure 3c). This assumes that the main part of the sand ribbon did not move during an experiment and only individual sand particles and clusters moved (i.e., the position of this starting line across the middle of the sand ribbon did not change during an experiment). Observations in the field and inspection of the photos confirmed this (e.g., in Figure 3, the shape of the sand ribbon and its  
330 position relative to the rocks remained the same). Based on these starting lines from the classified images, relative measures describing how far the sand moved can be calculated.

More specifically, the starting line in each classified image (pre- and post-experiment) was defined as follows. For every point across the slope (i.e., each individual pixel column  $i$  in the classified image), we determined a window of 101 pixels wide (50 pixel columns on each side, representing a 10.1 cm wide section on the plot) and counted the number of pixels that were  
335 classified as sand for each row (i.e., every 1 mm upslope from the gutter) within this window. The row with the highest number

of classified pixels was considered the starting line for column  $i$  and thus the starting point for sand movement. In case there were several maxima, the median row height was taken as the starting point. If there were only a few ( $< 30$ ) classified pixels, the value from the neighboring column was used to avoid breaks in the starting line (i.e., there were no gaps in the starting line, even if the sand ribbon itself had a small gap). At the left and right borders of the plot, the moving window was shorter to account for the lack of neighboring points on one side.

We used two measures to describe the movement of the sand during the sprinkling experiments: one related to the distance that the sand moved on the plot ( $\Delta D$ ) and the other to the area over which the sand ( $\Delta A$ ) moved. These two are clearly related to each other but can differ depending on the way that the sand moved across the plot. For each point across the plot (i.e., each column  $i$  in the classified images), we determined the distance ( $x_i$ ) between the starting line and the lowermost pixel that was classified as sand (Figure 4). We did this for the classified images taken before and after the experiments. The average value of this distance for the classified image taken before the sprinkling experiments represents approximately half of the width of the sand ribbon. Any change in this average distance for the classified image taken after the experiment is an indication of sand movement. This requires that the entire sand ribbon did not move downwards on the plots (which we did not observe, see Figure 3). Because the sand did not move at most points across the slope, we put extra weight on the particles that were located far from the starting line by using the root of the mean squared maximum distance for each column:

$$D = \sqrt{\frac{1}{n} * \sum_{i=1}^n x_i^2} \quad \text{Equation 1}$$

where  $i$  represents the location across the slope (i.e., the column number in the classified image) and  $n$  the total number of pixels across the plot (i.e., the total number of columns). To calculate how the mean root squared distance  $D$  changed from pre- to post experiment images, and thus to obtain a measure of the distance that the sand moved during an experiment, the percent change in  $D$  ( $\Delta D$ ) was calculated:

$$\Delta D = \left( \frac{D_{post}}{D_{pre}} - 1 \right) * 100 \% \quad \text{Equation 2}$$

where  $D_{post}$  is the root of the mean squared distance of the sand to the ribbon after the sprinkling experiment and  $D_{pre}$  is the root of the mean squared distance of the sand prior to the sprinkling experiment, and  $\Delta D$  represents the percent change in the root of the mean squared distance (increase or decrease in %) of the sand relative to the middle line of the ribbon. A larger positive value of  $\Delta D$  indicates that more particles moved further away from the ribbon. A negative value  $\Delta D$  is also possible and indicates that the sand ribbon became narrower during the experiment. This is possible when sand moved away from the ribbon and was washed into the soil or hidden below vegetation or rocks. True negative distances are also possible due to upslope splash erosion. We did not use the absolute maximum distance or a certain percentile of the maximum distances that the sand moved from the starting line to describe the sand movement because these measures are more sensitive to the detection

365 of individual sand particles than our more integrative measure  $D$ . Neither of these approaches account for transport of the sand off the plots (i.e., into the OF gutters) but  $D$  is less sensitive to this than the absolute maximum transport distance.

As another (but clearly related) measure of the spread of the sand across the plots, we also determined the area with sand ( $A$ ; Figure 3d and 4c) and changes therein. We selected all pixels between the furthest downslope and upslope occurrence of sand for each column of the classified images. Sand particles located more than 20 cm above the starting line were not considered  
370 as they were most likely not part of the sand ribbon. To account for the fact that the sand particles probably did not move down the hillslope in a straight line, the uppermost and lowermost (i.e., furthest upslope and downslope) occurrence of sand for each column was calculated for a 41-column window (i.e., 20 columns on each side, representing 2 cm on the plot; Figure 4). In case of gaps in the sand ribbon, the interpolated starting line was used to merge all areas to one area (Figure 4). Similar to the calculation of the sand transport distances, the percent change in the area  $A$  ( $\Delta A$ ) was calculated (Eq. (2) but with the  $A$  instead  
375 of  $D$ ) to determine the change in the area over which the sand was spread during the sprinkling experiments. This  $\Delta A$  does not represent the actual area over which the sand moved during the experiments (and would overestimate it) but is used here as a measure to compare the spread of the sand during the different experiments on the different plots. A larger positive value of  $\Delta A$  means that the sand was more spread out across the plot during the experiments. A negative value of  $\Delta A$  means that the area of sand became smaller, e.g., because the sand moved and was washed into the soil or stored below vegetation and rocks,  
380 or moved off the plot (however, we only observed some fluorescent sand particles in the outflow).

### 3.4 Digital Surface Model and flow accumulation

A digital surface model (DSM) derived from drone images of the moraines (drone: senseFly eBee; camera: Sony Cyber-shot DSC-WX220), created using Pix4DMapper by WWI Umweltplanung und Geoinformatik GbR. It was used together with the  
385  $D_{\infty}$  routing algorithm of Tarboton (1997) in ArcMap (v10.6.1) to determine the potential direction of OF. The drone-based images had a spatial resolution of ~4 cm, which was considered acceptable for the comparison with the results of the movement of the fluorescent sand particles (see section 3.3). However, the DSM (and thus also the flow routing) are influenced by vegetation. Because the vegetation was short (< 5 cm, except for two shrubs on the 1860M and 1990L plot) and the plots were steep, this should not have affected the flow directions considerably. Still, we only qualitatively compared these topograph-  
390 ically derived flow pathways to the observed patterns of sediment movement and did not use them for any statistical analyses. The other drone (see section 3.1.1) only took pictures of the plots (not the entire moraine), and hence could not be used to create a DSM with higher spatial resolution.

### 3.5 Data analysis

395 To determine if the differences in the surface characteristics (vegetation cover, rock cover, surface roughness, aggregate stability, and  $K_{sat}$ ) for the five plots were statistically significant, we used the Kruskal-Wallis tests and Nemenyi post-hoc tests. To determine if the differences in the surface characteristics were significantly different between the two moraines, we used the Mann-Whitney test.

For each event, we determined the total OF, peak flow rate, sediment yield, and peak turbidity. To better compare the OF characteristics between the experiments with different rainfall intensities and amounts, we calculated the OF runoff ratio by dividing the OF amount by the rainfall amount. To determine if the differences in total OF, peak flow, sediment yield and peak turbidity for the five plots were statistically significant, we used the Kruskal-Wallis tests and Nemenyi post-hoc tests. We used Spearman rank correlation ( $r_s$ ) to determine the correlation between the surface characteristics and total OF, peak flow, sediment yield and peak turbidity. Similarly, we used Spearman rank correlation to describe the relation between the rainfall intensity and total OF, peak flow, sediment yield, peak turbidity, and the percent changes in sand distance ( $\Delta D$ ) and sand-covered area ( $\Delta A$ ). Due to the differences in slope, aspect, and position of the plots, as well as differences in rainfall intensity, we did not expect strong correlations between the individual variables. Therefore, we also used a multiple linear model to predict the change in sand distance and area, using the rainfall intensity as an additional variable. We used the model to identify the interaction between rainfall intensity and the plot characteristics for OF and sediment yield. For the analyses, we used a 0.05 level of significance and the software R (v4.0.5 – used with RStudio v1.4.1106), especially the packages: “stats” (R Core Team, 2021), “caret” (Kuhn, 2021), “PMCMRplus” (Pohlert, 2022), “rsq” (Zhang, 2020) and “ggplot2” (Wickham, 2016).

## 4 Results

### 4.1 Plot characteristics

#### 4.1.1 Slope and surface roughness

All five plots were relatively steep, with the average slope ranging from 18° on 1990L to 35° on 1860M (Table 1; Figure 5a). On average, the plots on the 1860 moraine were steeper than the 1990 moraine (29° vs. 26°). The differences between the median slopes of the plots ( $p = 5e-04$ ) and the two moraines ( $p = 4e-03$ ) were significant. The variability in the slope was largest for the 1990L plot and smallest for the 1990M plot (coefficient of variation (CV) of 0.41 and 0.16, respectively).

420 There was also a significant difference in the surface roughness between the plots ( $p = 0.01$ ; Figure 5b) and the moraines ( $p = 7e-03$ ). The tortuosity index increased significantly from the 1860 moraine (median: 0.32; range: 0.18 – 0.47) to the 1990 moraine (median: 0.39; range: 0.26 – 0.86). The variability in the tortuosity index values was largest for the 1860M plot and smallest for the 1990M plot (CV of 0.32 and 0.15, respectively).

#### 4.1.2 Soil aggregate stability

425 The aggregate stability of the top 10 cm of the soil (Figure 5c) differed significantly between the plots ( $p = 0.02$ ; Figure 5c), and increased significantly from the 1990 moraine to the 1860 moraine ( $p = 2e-03$ ). The median soil aggregate stability coefficient (SAC) was lowest for the 1990M plot (0.14) and highest for the 1860M plot (0.71). The variability in soil aggregate stability was largest for the 1990M plot and smallest for the 1860L plot (CV of 0.74 and 0.44, respectively).

#### 4.1.3 Saturated hydraulic conductivity

430 The median values of saturated hydraulic conductivity ( $K_{sat}$ ) ranged between  $1320 \text{ mm h}^{-1}$  (1860M) and  $6120 \text{ mm h}^{-1}$  (1990M) (Figure 5d) and were not significantly different between the five plots ( $p = 0.12$ ). The median  $K_{sat}$  was significantly lower for the 1860 moraine than the 1990 moraine (median values of  $1560 \text{ mm h}^{-1}$  and  $4320 \text{ mm h}^{-1}$ ,  $p = 0.04$ ).

#### 4.2 Overland flow, turbidity and sediment yield

435 OF was observed less frequently on the 1860 moraine (three of the six experiments) than on the 1990 moraine (seven of the nine experiments; Figure 6, Table 2). OF was not observed for any of the low intensity (LI) experiments on the 1860 plots but was observed for all high intensity (HI) experiments on these plots. For the 1990 moraine, OF was also observed for all HI experiments, but for the plots on the footslopes of the moraine (1990L and 1990H), OF was also observed for the low and mid intensity (LI and MI) experiments (Table 2). Except for the plots located at the footslopes of the 1990 moraine, the OF runoff ratio (total OF divided by total precipitation) was  $< 3\%$ . For the footslope plots (1990L and 1990H) it was 8-10%. The average  
440 OF amount (for all experiments on a moraine) was almost three times larger for the 1990 moraine (1.8 mm) than the 1860 moraine (0.7 mm). When looking only at the HI experiments that produced OF on all plots, this difference is smaller (2.6 mm for the 1990 moraine vs. 1.5 mm for the 1860 moraine, or 8 vs. 3 % of the applied rainfall). The total amount of OF was especially high for the 1990L plot (3.6 mm or 11 % of the applied rainfall during the HI experiment; 8.1 mm or 10 % of applied  
445 rainfall for all three experiments combined; Figure 6).

For the plots on the 1860 moraine, peak turbidity and total sediment yield were small (Figure 6). Peak turbidity and sediment yield increased with rainfall intensity and were highest during the HI experiments for the 1990L and 1990H plots located at the foot of the moraine. There was a significant positive correlation between the peak flow rate and peak turbidity (Figure 7a;  $r_s = 0.77$ ;  $p = 0.02$ ), as well as between the amount of OF and sediment yield (Figure 7b;  $r_s = 0.81$ ;  $p = 7e-04$ ). For the 1990H plot, the total OF amount did not increase from the low to high-intensity experiments (Table 2), but sediment yield did. The results for the unscaled OF and sediment yield are similar (Fig. S13 in Supp. Material).

### 4.3 Sand movement

#### 4.3.1 Patterns of sand movement and changes in sand-covered areas

455 Individual sand particles and small clusters of sand ( $< 1 \text{ cm}^2$ ) were detected below the sand ribbon on both the 1860L and 1860M plots (Figure 8). For the 1860L plot, sand movement was more widespread during the high intensity HI experiment (blue sand ribbon) than for the other experiments, as reflected by the larger areas covered by the sand for the HI experiment than the LI and MI experiments. Such large sand-covered areas were also observed for the 1990L and 1990M plots (Figure 8). For the 1990H plot, individual sand particles, small clusters and larger sand-covered areas were detected below the sand ribbons. However, compared to the 1990L and 1990M plots, hardly any sand moved on the 1990H plot. These qualitative differences in sand movement between the moraines are also reflected in the differences in the sand transport distances  $\Delta D$  ( $p = 3e-03$ ) and the change in the sand-covered areas  $\Delta A$  ( $p = 2e-03$ ; Figure 9, Table 2).

465 For five of the six experiments on the 1860 moraine, the change in sand-covered area was negative (i.e., the area covered with the fluorescent sand decreased during the experiment). The calculated sand transport distance was negative for four of the six experiments, also indicating the disappearance of the fluorescent sand (not an upslope transport). Such decreases indicate that the sand moved and was washed into the soil, hidden below rocks or vegetation. This was not observed for the experiments on the 1990 moraine (Figure 9). The decreases in  $\Delta D$  and  $\Delta A$  were largest for the LI experiment on the 1860L plot ( $\Delta D$ : -51 % and  $\Delta A$ : -52 %); the increases were largest for the 1990L plot (Figure 9).

#### 4.3.2 Comparison with the blue dye

470 The fluorescent sand and the blue dye on the 1990L plot were both transported to the bottom of the plots (Figure 8, Figure 10) and the flow pathways of the blue dye tracer matched the distribution of the sand-covered areas well (Figure 10a and b).. Sand and OF moved in four distinct areas, which matched the flow patterns derived from the DSM (Figure 10c). The first flow path (#1 in Figure 10) was located towards the left plot boundary (when looking upslope). The orange sand placed on the plot before the LI experiment was redistributed along this flow path. The second OF flow path (#2 in Figure 10) was located further down and slightly to the left. Sand particles from all three sand ribbons were found here, suggesting that OF occurred here during all three experiments. The third pathway (#3 in Figure 10) is mainly characterized by ponding in the slightly flatter area of the plot. In this microtopographic depression, the blue sand from the HI experiment was deposited. A fourth OF pathway (#4 in Figure 10) was observed during all experiments and all three sand colors were found in this region.

### 4.4 Relation between overland flow, sand movement and plot characteristics

480 There was no significant correlation between the percent changes in sand-covered area  $\Delta A$  and either total OF ( $r_s = 0.51$ ;  $p = 0.07$ ), the OF runoff ratio ( $r_s = 0.52$ ;  $p = 0.05$ ), peak flow rate ( $r_s = 0.34$ ;  $p = 0.40$ ), peak turbidity ( $r_s = 0.52$ ;  $p = 0.09$ ), sediment yield ( $r_s = 0.56$ ;  $p = 0.09$ ), or sediment yield per unit rainfall ( $r_s = 0.58$ ;  $p = 0.08$ ; Figure 11). This was mainly due to the fact that for some experiments, no OF was measured at the bottom of the plot but there were changes in the sand-covered



area. If these events are excluded from the analyses, a higher percent change in the sand-covered area corresponded to more  
485 OF, a higher OF runoff ratio, a higher peak OF rate, peak turbidity, sediment yield, and sediment yield per unit rainfall (Figure  
11). Relations with the sand transport distance  $\Delta D$  were similar to those for the change in sand covered area (see Figure S11  
in Supplementary Material).

The percent change in sand-covered area ( $r_s = 0.77$ ;  $p = 7e-04$ ; Figure 12g), the OF runoff ratio ( $r_s = 0.78$ ;  $p = 6e-04$ ; Figure  
12a), total OF ( $r_s = 0.66$ ;  $p = 7e-03$ ), and sediment yield ( $r_s = 0.62$ ;  $p = 0.01$ ; Figure 12d) were all significantly and positively  
490 correlated to the surface rock cover. The percent change in sand-covered area ( $r_s = 0.55$ ;  $p = 0.03$ ; Figure 12i), OF runoff ratio  
( $r_s = 0.54$ ,  $p = 0.04$ ; Figure 12c), total OF ( $r_s = 0.54$ ;  $p = 0.04$ ) and rock cover ( $r_s = 0.53$ ;  $p = 0.03$ ) were also significantly and  
positively correlated to the surface roughness (i.e., tortuosity index). The percent change in sand-covered area was negatively  
correlated to the vegetation cover ( $r_s = -0.57$ ;  $p = 0.03$ ; Figure 12h) and positively correlated to  $K_{sat}$  ( $r_s = 0.62$ ;  $p = 0.02$ ).

The multiple linear model indicated that rock cover, vegetation cover, and their interaction with the rainfall intensity could  
495 predict the total OF ( $R^2 = 0.64$ ; Root Mean Squared Error (RMSE) = 0.6 mm) and sediment yield ( $R^2 = 0.77$ ; RMSE = 5.2 g)  
reasonably well but these plot characteristics were not very suitable predictors for the percent change in sand-covered area ( $R^2$   
= 0.35; RMSE = 70 %).

## 5 Discussion

### 500 5.1 Advantages and disadvantages of the fluorescent sand to study sediment transport

The results of this study suggest that fluorescent sand can be useful to assess sediment transport on natural hillslopes with  
coarse soils and little vegetation (Figure 10). In particular, it provided information on the movement of particles on the plot.  
A main benefit of the sand tracer method is that very local and short sediment transport distances are identifiable. Thus, some  
information on OF and soil erosion can be obtained, even if no OF is detected below the plots. The distribution of the fluores-  
505 cent sand particles matched that of the blue dye and provides information on the locations of infiltration of OF and deposition  
of the sediment, and thus the identification of local deposition areas or sinks (e.g., pathway #3 in Figure 10). For two experi-  
ments (LI, MI) on the 1990M plot, there was considerable sediment movement, even-though no OF was recorded. This sedi-  
ment movement would not have been known if there were only measurements at the bottom of the plot (and also explains the  
lack of the correlation between sediment yield and sand movement (Figure 11d)). The movement of the sand thus highlighted  
510 the importance of re-infiltration of OF on this plot. In other words, the fluorescent sand can help us to understand where  
sediment transport occurs and thus provide information about functional connectivity. The related disadvantage of the fluores-  
cent sand method is that it only describes the local movement of fluorescent sand particles (i.e., plot scale movement) and can

not be used to predict sediment yield at the bottom of the plot. For sediment yield, the particles need to travel at least to the bottom of the plot, which was not the case for several of our experiments.

515 The fluorescent sand method is well suited to study sediment transport on poorly vegetated soils that contain a significant amount of sand (i.e., have a similar grain size as the sand tracer). In other words, it is well suited for coarse hillslopes in high alpine regions, dunes, etc. However, the sand does not move exactly like the soil. The fluorescent sand was loose and did not represent natural soil aggregates. On soils with finer textured material, the method will no longer represent the detachment and transport of the natural soil particles.

520 The detection of the sand would have been possible without the use of the LED-lamps or with a common fluorescent tracer without afterglow effect (as used by Hardy et al., 2019, 2017, 2016; Tauro et al., 2016, 2012a, 2012b; Young and Holt, 1968). However, the use of a glow in the dark sand that emits light for several minutes without a light source is a considerable advantage for very rough surfaces, where vegetation or rocks lead to shading and some of the sand particles cannot be seen directly. By moving the LED-light and UV-light sources around the plot before taking the photos, it was possible to see these  
525 particles due to their afterglow. On young moraines where the surfaces are rough, this is particularly useful.

An advantage of the fluorescent sand is that it can be used to study sediment transport during natural rainfall events (although we didn't do this). Many of the previous studies that have described OF pathways required real-time observations of the water or the tracer. To automate data collection during the event, they measured water temperatures with thermal cameras (Lima et al., 2015) or recorded videos for particle detection on beaches, rivers, or hillslopes (Tauro et al., 2012a, b, 2016; Hardy et al.,  
530 2017, 2016). This requirement for photographs or videos during the event means that the tracer can only be used during sprinkling experiments or at places where the timing of sediment transport is predictable (e.g., on the beach). The advantage of the fluorescent sand method, as presented here, is that it does not require a real-time particle detection or tracking system. It means that the particles can, at least in theory, be applied to a surface and photographs can be taken before and after the rainfall event, so that fully natural conditions can be studied. This is especially useful in remote or exposed locations, when the occurrence  
535 of the next natural rainfall event is unknown, and where experiments need to be done on multiple plots simultaneously and it is too expensive to equip each plot with a camera. If equipment is available, real-time particle tracking has the advantage that it also provides information on when sediment transport occurs and can record the actual water flow.

The dissolution of the glue was a disadvantage of the fluorescent sand that we used. Despite being listed as waterproof, the sand formed aggregates (1 – 15 mm in size) after a wetting and drying cycle. The aggregates were rather stable, indicating that  
540 parts of the glue that bonds the photoluminescent tracer powder on the sand particles dissolved during the sprinkling experiments and bound with other particles, mainly other (i.e., neighboring) fluorescent sand particles, after drying. In the following sprinkling experiments, such “glue induced aggregates” were barely broken up and were thus unlikely to be transported (although there was still some transport). As a result, the fluorescent sand that we used can only be used to determine sediment

transport for the first event after an application (as we did). This is a disadvantage because it requires application before the  
545 event of interest. The advantage is that there is more time to take the photographs after the event because the pattern will not  
change considerably due to a second event. Another type of fluorescent sand should be used to study sediment transport during  
multiple events. We did not observe washed off tracer powder on natural sand particles that would create “fake particles”.  
Also, no photo-quenching effects or changes in the color were observed between the pre and post event photos. Even if there  
would have been small changes in the color, these would not have had an effect as the typical color range for each sand was  
550 determined based on the pre and post experiment photos separately.

We consider the method used in this study applicable for the microscale (several centimeters) to plot scale (several meters)  
experiments but do not recommend its use for larger scales. First, the image resolution would become too coarse. With a  
modified setup one could study sediment transport at larger scales, e.g., one could use the camera at different locations (to  
monitor different areas of the hillslope) and stitch the photos together or use a camera on a rail that takes several pictures of  
555 the hillslope. Second, on larger plots or longer hillslopes, the sand is more likely to get stuck behind rocks and vegetation, so  
that it is unlikely to be observed far from the applied ribbon. However, this provides interesting information to understand  
sediment transport distances and connectivity as well. A solution could be the use of multiple sand ribbons of different colors.

Another disadvantage of our approach was the movement and sagging of the fluorescent segmented chain as a reference  
marker. A solution would be the use of long and stable nails or pistons with fluorescent tips that are anchored deep into the  
560 soil and thus representing more stable reference points. With more stable reference points, it would be possible to compare the  
pre- and post-event images more directly (although also here, uncertainties in the georeferencing can introduce errors).

## **5.2 Effects of surface characteristics on overland flow and sand movement**

The results of this study provide valuable information regarding OF generation and sediment transport on young moraines and  
565 how this changes during initial landscape development, but also need to be interpreted with caution as the number of experi-  
ments and observations are very small. The significant differences in the total amount of OF and OF runoff ratios between the  
1860 and 1990 moraines (Figure 6) highlight the changes in the partitioning of rainfall into OF and infiltration (see also Maier  
et al., 2020) and sediment transport during landscape evolution. Vegetation cover (Greinwald et al., 2021a), root density  
(Greinwald et al., 2021b), and macroporosity (Hartmann et al., 2020a) increase during landscape evolution. The plots on the  
570 1860 moraine were also characterized by a smoother surface than the 1990 moraine (Maier and van Meerveld, 2022), were  
dominated by grassland vegetation with a dense root networks and macropores close to the surface that promote infiltration  
(cf. Hino et al., 1987; Ding and Li, 2016; Greinwald et al., 2021b). On the plots on the 1860 moraine, most sand polygons  
were small and parts of the sand disappeared during the experiments (Figure 8, Figure 9 and Table 2), which suggests vertical  
transport (translocation) of the sand particles (and water) into the macroporous topsoil, or at least below the vegetation. The

575 vegetation protects the soil particles from detachment (Geißler et al., 2012; Gyssels et al., 2005) and acts as a barrier that traps eroded sediment (Wainwright et al., 2000; Rey, 2003; Pearce et al., 1997; Marchamalo et al., 2016). The negative values for  $\Delta D$  and  $\Delta A$  for the plots on the 1860 moraine are, thus, mainly caused by the higher vegetation cover and macroporosity compared to the 1990 moraine (cf. Ehabu et al., 2018; Marques et al., 2007; Mu et al., 2019; Rey et al., 2004; Zhang et al., 2004).

580 The observed difference in total OF between the moraines and plots explains the difference in sediment yield (Figure 6, Figure 7b) and the redistribution of the fluorescent sand (Figure 8, Figure 10). The plot with the most OF also had the largest overall sediment yield (1990L). This is not surprising as the importance of OF for soil erosion has been recognized for decades (e.g., Farmer, 1971; Knapen et al., 2007; Komura, 1976; Parsons, 1992; Poesen, 2017; Singer and Walker, 1983), even if other factors, such as the geotechnical properties of moraine sediments, also play an important role for slope stability, soil erosion and sediment transport (Curry et al., 2009). The transport of the fluorescent sand below the ribbons (Figure 8), however, also highlights that even if no OF is measured at the bottom of the plot (Figure 6), there may still be local OF and transport of sediment on the plot (Figure 8, Figure 9). Nonetheless, in these cases, connectivity to the bottom of the plot is low. Connectivity on larger scales (e.g., hillslope scale) may also be even more different as OF may infiltrate or exfiltrate as return flow, depending on downslope contributing areas and the connection of saturated areas along the flowpaths (see e.g., analyses of Lane et al. (2004, 2009) based on the topographic wetness index (TWI)).

590

The correlations between the surface characteristics and OF and sediment yield (Figure 12) and the results of the multiple linear model suggest that the high rock- and stone cover on the 1990 moraine led to considerable OF generation. Rock cover and sand content decrease with moraine age due to the effects of physical and chemical weathering (Musso et al., 2019 and 2022; Maier et al., 2020). In alpine terrain, the effects of physical weathering due to congelifraction can be particularly fast.

595 The rapid change in texture causes the  $K_{sat}$  to decrease during initial soil development, even though root density increases (Maier et al., 2020). However, in the areas covered with rocks (Figure S12 in Supplementary Material), infiltration is limited, leading to the generation of OF. Where this water infiltrates between the rocks, the sand particles are deposited on the surface or washed into the soil. This mainly occurred in the slightly flatter areas, behind vegetation patches, and behind rocks (e.g., flowpath #3 in Figure 10). Quicker and more pronounced OF responses on hillslopes with large rock- and stone cover have

600 been reported by others (e.g., Lavee and Poesen, 1991; Poesen et al., 1990; Poesen and Lavee, 1994). The positive, rather than negative, correlation between  $K_{sat}$  and sediment transport (chapter 4.4) can be explained by the fact that  $K_{sat}$  was measured for the sediment between the rocks and not on the impermeable areas of the large rocks. The plot-average surface infiltration is much lower for the 1990 moraine than the 1860 moraine due to the higher rock cover. The substantially higher OF on the 1990 moraine plots is also influenced by the position of the two plots at the footslope of the 1990 moraine, which caused the soils

605 to be wetter and promoted saturated overland flow (Maier et al., 2021).

The rocks and stones on the 1990 moraine are also responsible for the higher surface roughness. A high surface roughness can reduce sediment connectivity and provide places where ponding occurs and OF infiltrates, and thus sinks for the sediment that it carries, preventing further downslope flow and transport (Thompson et al., 2010a; Dunkerley, 2003; Johnson et al., 1979; Jomaa et al., 2012). However, other studies (e.g., Darboux and Huang, 2005; Dunkerley, 2004; Helming et al., 1998) have reported a positive correlation between surface roughness, OF generation and connectivity because surface roughness concentrates the flow and accelerates the flow of water in downslope-orientated structures. This flow can promote sediment transport and enhance erosion (Liu and Singh, 2004). We assume that this was the case for the plots of the 1990 moraine, where the OF pathways (as visualized by the blue dye) indeed followed microtopographic depressions with a downslope orientation (Figure 10). The strong overlap between the redistribution of the fluorescent sand (sand polygons) and the pathways of the blue dye allowed the identification of the areas where OF occurred and where OF re-infiltrated (Figure 10). However, the opposite is not true: a lack of sediment movement should not be interpreted as an absence of surface water flow. Water and sediment movement can be disconnected (e.g., where the transport capacity of the water is too low to move the sediment, where OF infiltrates into the soil and then exfiltrates again, or where splash erosion is important). Also, OF that is generated close to the gutters (and thus far below the sand ribbon) would not have caused any movement of the fluorescent sand. Furthermore, not all of the sand movement can be attributed to OF-driven soil erosion. The different patterns of sand movement (isolated small clusters, aggregates or even single sand particles vs. more connected parts covered by fluorescent sand) indicate the influence of splash erosion. Recorded maximum splash distances for sand particles with a similar diameter as the fluorescent sand used in this study (300 – 500  $\mu\text{m}$ ) are  $\sim 45$  cm for rainfall intensities of  $\sim 30$   $\text{mm hr}^{-1}$  and a median raindrop size of  $\sim 1.4$  mm (Legout et al., 2005), suggesting that some of the particles may have moved by splash erosion as well.

## 6 Conclusions

We tested the use of fluorescent sand with an afterglow in combination with sprinkling experiments to study sediment transport on young moraines in the Swiss Alps. Although fluorescent particles have been used in previous studies, in particular in flume experiments, this study highlights the potential of using fluorescent sand with an afterglow to identify and quantify sediment transport on natural hillslopes. The afterglow of the fluorescent sand improves the visibility of the sand on rough surfaces, such as in proglacial areas. The main advantage of the fluorescent sand as a tracer to study sediment movement is that it shows the redistribution of sediment on the plot, and thus provides information on sediment movement even if no overland flow is observed at the bottom of the plot. Another advantage is that the sand is cheap and that no photos or videos need to be taken during the experiment, making it logistically easier to study sediment transport during events and on multiple plots.

The fluorescent sand was transported to distinct areas on the plots that matched the pathways of the overland flow during a blue dye staining experiment. The redistribution of the fluorescent sand also highlighted the differences in sediment transport

processes for the two moraines. The more extensive vegetation cover on the older moraine protected the surface from splash detachment and transport and also promoted infiltration of OF and sediment into near-surface macropores and other preferential flow paths. In contrast, the high rock cover on the younger moraine led to concentrated overland flow pathways and larger sediment transport distances, and for some experiments, a high sediment yield. These observations highlight the importance of microtopography on sediment transport and the importance of re-infiltration of overland flow and deposition of sediment behind vegetation patches and rocks, as well as the changes in sediment transport during the initial years of landscape evolution.

## 7 Code and data availability

The data described in this article can be downloaded from: Maier, F. and van Meerveld, I.: HILLSCAPE Project - Data on moraine soil properties and on overland flow and subsurface flow characteristics. GFZ Data Services.

<https://doi.org/10.5880/figeo.2021.011>, 2021.

The code to analyze the photos is available from the first corresponding author on request.

## 8 Author contribution

IvM came up with the idea and formulated the overarching research goals together with FM and FL. IvM, FM and FL developed the methodology and the design of the study. FM and FL did the fieldwork and collected the data. FL was responsible for the fluorescent sand photographs and analysis, FM for the sprinkling experiments, OF, sediment and turbidity measurements. FM and FL wrote the initial draft of the manuscript and the codes to analyse the data, and IvM reviewed and edited the draft of the manuscript. FM and FL created all figures with feedback from IvM. IvM acquired the funding for the study, field materials, laboratory equipment and computing resources.

## 9 Competing interests

The authors declare no competing interests. The authors have no involvement or financial interest in Noxton Technologies, the supplier of the fluorescent sand.

## 10 Acknowledgements

This research was funded by the Swiss National Science Foundation (SNSF; project grant number 200021E-167563/1) and the German Research Foundation (DFG; project number 318089487) and is part of the HILLSCAPE project ([www.hillscape.ch](http://www.hillscape.ch)).

We thank all members of the HILLSCAPE team, including the MSc. students, BSc. students, interns and staff who were involved in the design of the rainfall experiments and data collection. We, furthermore, thank the Alpin Center Sustenpass,

665 and in particular Thomas Michel, for logistical support, meals and accommodation during the fieldwork. Many thanks to Peter  
Luchs and the Kraftwerke Oberhasli AG for the permission to conduct fieldwork on their property and the provision of tools.

## 11 References

- Anache, J. A. A., Flanagan, D. C., Srivastava, A., and Wendland, E. C.: Land use and climate change impacts on runoff and  
670 soil erosion at the hillslope scale in the Brazilian Cerrado, *Sci. Total Environ.*, 622–623, 140–151,  
<https://doi.org/10.1016/j.scitotenv.2017.11.257>, 2018.
- Angulo-Martínez, M., Beguería, S., Navas, A., and Machín, J.: Splash erosion under natural rainfall on three soil types in NE  
Spain, 175–176, 38–44, <https://doi.org/10.1016/j.geomorph.2012.06.016>, 2012.
- Appels, W. M., Bogaart, P. W., and van der Zee, S. E. A. T. M.: Influence of spatial variations of microtopography and  
675 infiltration on surface runoff and field scale hydrological connectivity, *Adv. Water Resour.*, 34, 303–313,  
<https://doi.org/10.1016/j.advwatres.2010.12.003>, 2011.
- Appels, W. M., Bogaart, P. W., and van der Zee, S. E. A. T. M.: Surface runoff in flat terrain: How field topography and runoff  
generating processes control hydrological connectivity, *J. Hydrol.*, 534, 493–504,  
<https://doi.org/10.1016/j.jhydrol.2016.01.021>, 2016.
- 680 Asadi, H., Shahedi, K., Jarihani, B., and Sidle, R.: Rainfall-Runoff Modelling Using Hydrological Connectivity Index and  
Artificial Neural Network Approach, 11, 212, <https://doi.org/10.3390/w11020212>, 2019.
- Badr, A. A. and Lotfy, M. F.: Tracing beach sand movement using fluorescent quartz along the Nile delta promontories, Egypt,  
*J. Coast. Res.*, 15, 261–265, 1999.
- Bast, A., Wilcke, W., Graf, F., Lüscher, P., and Gärtner, H.: A simplified and rapid technique to determine an aggregate  
685 stability coefficient in coarse grained soils, 127, 170–176, <https://doi.org/10.1016/j.catena.2014.11.017>, 2015.
- Bertuzzi, P., Rauws, G., and Courault, D.: Testing roughness indices to estimate soil surface roughness changes due to  
simulated rainfall, *Soil Tillage Res.*, 17, 87–99, [https://doi.org/https://doi.org/10.1016/0167-1987\(90\)90008-2](https://doi.org/https://doi.org/10.1016/0167-1987(90)90008-2), 1990.
- Blanchard, D. C.: Raindrop size-distribution in Hawaiian rains, *J. Meteorol.*, 10, 457–473, [https://doi.org/10.1175/1520-0469\(1953\)010<0457:RSDIHR>2.0.CO;2](https://doi.org/10.1175/1520-0469(1953)010<0457:RSDIHR>2.0.CO;2), 1953.
- 690 Bracken, L. J. and Croke, J.: The concept of hydrological connectivity and its contribution to understanding runoff-dominated  
geomorphic systems, *Hydrol. Process.*, 21, 1749–1763, <https://doi.org/10.1002/hyp.6313>, 2007.
- Bracken, L. J., Wainwright, J., Ali, G. A., Tetzlaff, D., Smith, M. W., Reaney, S. M., and Roy, A. G.: Concepts of hydrological  
connectivity: Research approaches, pathways and future agendas, *Earth-Science Rev.*, 119, 17–34,  
<https://doi.org/10.1016/j.earscirev.2013.02.001>, 2013.
- 695 Brardinoni, F. and Hassan, M. A.: Glacial erosion, evolution of river long profiles, and the organization of process domains in  
mountain drainage basins of coastal British Columbia, *J. Geophys. Res.*, 111, F01013,  
<https://doi.org/10.1029/2005JF000358>, 2006.
- Brighenti, S., Tolotti, M., Bruno, M. C., Wharton, G., Pusch, M. T., and Bertoldi, W.: Ecosystem shifts in Alpine streams  
under glacier retreat and rock glacier thaw: A review, *Sci. Total Environ.*, 675, 542–559,  
700 <https://doi.org/10.1016/j.scitotenv.2019.04.221>, 2019.
- Buda, A. R., Kleinman, P. J. A., Srinivasan, M. S., Bryant, R. B., and Feyereisen, G. W.: Factors influencing surface runoff  
generation from two agricultural hillslopes in central Pennsylvania, *Hydrol. Process.*, 23, 1295–1312,  
<https://doi.org/10.1002/hyp.7237>, 2009.
- Buendia, C., Vericat, D., Batalla, R. J., and Gibbins, C. N.: Temporal Dynamics of Sediment Transport and Transient In-

- 705 channel Storage in a Highly Erodible Catchment, *L. Degrad. Dev.*, 27, 1045–1063, <https://doi.org/10.1002/ldr.2348>, 2016.
- Calsamiglia, A., Gago, J., Garcia-Comendador, J., Bernat, J. F., Calvo-Cases, A., and Estrany, J.: Evaluating functional connectivity in a small agricultural catchment under contrasting flood events by using UAV, *Earth Surf. Process. Landforms*, 45, 800–815, <https://doi.org/10.1002/esp.4769>, 2020.
- 710 Cammeraat, L. H.: A review of two strongly contrasting geomorphological systems within the context of scale, *Earth Surf. Process. Landforms*, 27, 1201–1222, <https://doi.org/10.1002/esp.421>, 2002.
- Carnahan, E., Amundson, J. M., and Hood, E.: Impact of glacier loss and vegetation succession on annual basin runoff, *Hydrol. Earth Syst. Sci.*, 23, 1667–1681, <https://doi.org/10.5194/hess-23-1667-2019>, 2019.
- Coles, A. E. and McDonnell, J. J.: Fill and spill drives runoff connectivity over frozen ground, *J. Hydrol.*, 558, 115–128, <https://doi.org/10.1016/j.jhydrol.2018.01.016>, 2018.
- 715 Colombo, N., Salerno, F., Martin, M., Malandrino, M., Giardino, M., Serra, E., Godone, D., Said-Pullicino, D., Fratianni, S., Paro, L., Tartari, G., and Freppaz, M.: Influence of permafrost, rock and ice glaciers on chemistry of high-elevation ponds (NW Italian Alps), *Sci. Total Environ.*, 685, 886–901, <https://doi.org/10.1016/j.scitotenv.2019.06.233>, 2019.
- Cowie, N. M., Moore, R. D., and Hassan, M. A.: Effects of glacial retreat on proglacial streams and riparian zones in the Coast and North Cascade Mountains, *Earth Surf. Process. Landforms*, 39, 351–365, <https://doi.org/10.1002/esp.3453>, 2014.
- 720 Curry, A. M., Sands, T. B., and Porter, P. R.: Geotechnical controls on a steep lateral moraine undergoing paraglacial slope adjustment. Geological Society, London, Special Publications, 320(1), 181–197. <https://doi.org/10.1144/SP320.12>, 2009.
- Darboux, F. and Huang, C.: Does Soil Surface Roughness Increase or Decrease Water and Particle Transfers?, *Soil Sci. Soc. Am. J.*, 69, 748–756, <https://doi.org/10.2136/sssaj2003.0311>, 2005.
- 725 Deasy, C. and Quinton, J. N.: Use of rare earth oxides as tracers to identify sediment source areas for agricultural hillslopes, 1, 111–118, <https://doi.org/10.5194/se-1-111-2010>, 2010.
- Ding, W. and Li, M.: Effects of grass coverage and distribution patterns on erosion and overland flow hydraulic characteristics, *Environ. Earth Sci.*, 75, 477, <https://doi.org/10.1007/s12665-016-5329-7>, 2016.
- 730 Dorador, J., Rodríguez-Tovar, F.J. and Expedition, I.O.D.P.: Quantitative estimation of bioturbation based on digital image analysis. *Marine Geology*, 349, pp.55-60, <https://doi.org/10.1016/j.margeo.2014.01.003>, 2014.
- Dunkerley, D.: Flow threads in surface run-off: implications for the assessment of flow properties and friction coefficients in soil erosion and hydraulics investigations, *Earth Surf. Process. Landforms*, 29, 1011–1026, <https://doi.org/10.1002/esp.1086>, 2004.
- 735 Dunkerley, D. L.: Determining friction coefficients for interrill flows: the significance of flow filaments and backwater effects, *Earth Surf. Process. Landforms*, 28, 475–491, <https://doi.org/10.1002/esp.453>, 2003.
- Dunne, T., Zhang, W., and Aubry, B. F.: Effects of Rainfall, Vegetation, and Microtopography on Infiltration and Runoff, *Water Resour. Res.*, 27, 2271–2285, <https://doi.org/10.1029/91WR01585>, 1991.
- Ebabu, K., Tsunekawa, A., Haregeweyn, N., Adgo, E., Meshesha, D. T., Aklog, D., Masunaga, T., Tsubo, M., Sultan, D., 740 Fenta, A. A., and Yibeltal, M.: Analyzing the variability of sediment yield: A case study from paired watersheds in the Upper Blue Nile basin, Ethiopia, 303, 446–455, <https://doi.org/10.1016/j.geomorph.2017.12.020>, 2018.
- Eigel, J. and Moore, I. D.: A simplified technique for measuring raindrop size and distribution, *Trans. ASAE*, 26, 1079–1084, 1983.
- Evans, R.: Mechanics of ater erosion and their spatial and temporal controls: an empirical viewpoint., *Soil Erosion*. Wiley, 745 Chichester, 109–128, 1980.
- Farmer, E. E.: Soil erosion by overland flow and raindrop splash on three mountain soils, (No. 92-10., Intermountain Forest & Range Experiment Station, Forest Service, US Department of Agriculture., 1971.



- Fernández-Raga, M., Palencia, C., Keesstra, S., Jordán, A., Fraile, R., Angulo-Martínez, M., and Cerdà, A.: Splash erosion: A review with unanswered questions, *Earth-Science Rev.*, 171, 463–477, <https://doi.org/10.1016/j.earscirev.2017.06.009>, 2017.
- 750 Garnier, E., Navas, M. L., and Grigulis, K.: *Plant functional diversity: organism traits, community structure, and ecosystem properties*, Oxford University Press, 2016.
- Gay, A., Cerdan, O., Mardhel, V., and Desmet, M.: Application of an index of sediment connectivity in a lowland area, *J. Soils Sediments*, 16, 280–293, <https://doi.org/10.1007/s11368-015-1235-y>, 2016.
- 755 Geilhausen, M., Morche, D., Otto, J.-C., and Schrott, L.: Sediment discharge from the proglacial zone of a retreating Alpine glacier, *Zeitschrift für Geomorphol. Suppl. Issues*, 57, 29–53, <https://doi.org/10.1127/0372-8854/2012/S-00122>, 2013.
- Geißler, C., Lang, A. C., von Oheimb, G., Härdtle, W., Baruffol, M., and Scholten, T.: Impact of tree saplings on the kinetic energy of rainfall—The importance of stand density, species identity and tree architecture in subtropical forests in China, *Agric. For. Meteorol.*, 156, 31–40, <https://doi.org/10.1016/j.agrformet.2011.12.005>, 2012.
- 760 Gerke, K. M., Sidle, R. C., and Mallants, D.: Preferential flow mechanisms identified from staining experiments in forested hillslopes, *Hydrol. Process.*, 29, 4562–4578, <https://doi.org/10.1002/hyp.10468>, 2015.
- Gianinetto, M., Aiello, M., Vezzoli, R., Polinelli, F. N., Rulli, M. C., Chiarelli, D. D., Bocchiola, D., Ravazzani, G., and Soncini, A.: Future Scenarios of Soil Erosion in the Alps under Climate Change and Land Cover Transformations Simulated with Automatic Machine Learning, 8, 28, <https://doi.org/10.3390/cli8020028>, 2020.
- 765 van De Giesen, N. C., Stomph, T. J., and de Ridder, N.: Scale effects of Hortonian overland flow and rainfall-runoff dynamics in a West African catena landscape, *Hydrol. Process.*, 14, 165–175, [https://doi.org/10.1002/\(SICI\)1099-1085\(200001\)14:1<165::AID-HYP920>3.0.CO;2-1](https://doi.org/10.1002/(SICI)1099-1085(200001)14:1<165::AID-HYP920>3.0.CO;2-1), 2000.
- Gobiet, A. and Kotlarski, S.: Future Climate Change in the European Alps, *Oxford Res. Encycl. Clim. Sci.*, 1–22, <https://doi.org/10.1093/acrefore/9780190228620.013.767>, 2020.
- 770 Gobiet, A., Kotlarski, S., Beniston, M., Heinrich, G., Rajczak, J., and Stoffel, M.: 21st century climate change in the European Alps-A review, *Sci. Total Environ.*, 493, 1138–1151, <https://doi.org/10.1016/j.scitotenv.2013.07.050>, 2014.
- Govers, G., Takken, I., and Helming, K.: Soil roughness and overland flow, 20, 131–146, <https://doi.org/10.1051/agro:2000114>, 2000.
- 775 Greinwald, K., Gebauer, T., Treuter, L., Kolodziej, V., Musso, A., Maier, F., Lustenberger, F., and Scherer-Lorenzen, M.: Root density drives aggregate stability of soils of different moraine ages in the Swiss Alps, *Plant Soil*, <https://doi.org/10.1007/s11104-021-05111-8>, 2021a.
- Greinwald, K., Dieckmann, L. A., Schipplick, C., Hartmann, A., Scherer-Lorenzen, M., and Gebauer, T.: Vertical root distribution and biomass allocation along proglacial chronosequences in Central Switzerland, Arctic, Antarct. Alp. Res., 53, 20–34, <https://doi.org/10.1080/15230430.2020.1859720>, 2021b.
- 780 Guzmán, G., Barrón, V., and Gómez, J. A.: Evaluation of magnetic iron oxides as sediment tracers in water erosion experiments, 82, 126–133, <https://doi.org/10.1016/j.catena.2010.05.011>, 2010.
- Guzmán, G., Laguna, A., Cañasveras, J. C., Boulal, H., Barrón, V., Gómez-Macpherson, H., Giráldez, J. V., and Gómez, J. A.: Study of sediment movement in an irrigated maize–cotton system combining rainfall simulations, sediment tracers and soil erosion models, *J. Hydrol.*, 524, 227–242, <https://doi.org/10.1016/j.jhydrol.2015.02.033>, 2015.
- 785 Gysels, G., Poesen, J., Bochet, E., and Li, Y.: Impact of plant roots on the resistance of soils to erosion by water: a review, *Prog. Phys. Geogr. Earth Environ.*, 29, 189–217, <https://doi.org/10.1191/0309133305pp443ra>, 2005.
- Hachani, S., Boudevillain, B., Delrieu, G., and Bargaoui, Z.: Drop size distribution climatology in Cévennes-Vivarais region, France, *Atmosphere (Basel)*, 8, <https://doi.org/10.3390/atmos8120233>, 2017.
- 790 Harden, C. P. and Scruggs, P. D.: Infiltration on mountain slopes: a comparison of three environments, 55, 5–24,

[https://doi.org/10.1016/S0169-555X\(03\)00129-6](https://doi.org/10.1016/S0169-555X(03)00129-6), 2003.

- Hardy, R. A., Pates, J. M., Quinton, J. N., and Coogan, M. P.: A novel fluorescent tracer for real-time tracing of clay transport over soil surfaces, 141, 39–45, <https://doi.org/10.1016/j.catena.2016.02.011>, 2016.
- Hardy, R. A., James, M. R., Pates, J. M., and Quinton, J. N.: Using real time particle tracking to understand soil particle movements during rainfall events, 150, 32–38, <https://doi.org/10.1016/j.catena.2016.11.005>, 2017.
- 795 Hardy, R. A., Quinton, J. N., James, M. R., Fiener, P., and Pates, J. M.: High precision tracing of soil and sediment movement using fluorescent tracers at hillslope scale, *Earth Surf. Process. Landforms*, 44, 1091–1099, <https://doi.org/10.1002/esp.4557>, 2019.
- Hartmann, A., Semenova, E., Weiler, M., and Blume, T.: Field observations of soil hydrological flow path evolution over 10  
800 Millennia, *Hydrol. Earth Syst. Sci.*, 28, 1–26, <https://doi.org/10.5194/hess-2020-28>, 2020a.
- Hartmann, A., Weiler, M., and Blume, T.: The impact of landscape evolution on soil physics: Evolution of soil physical and hydraulic properties along two chronosequences of proglacial moraines, *Earth Syst. Sci. Data*, 1–26, <https://doi.org/10.5194/essd-2020-110>, 2020b.
- Heckmann, T. and Schwanghart, W.: Geomorphic coupling and sediment connectivity in an alpine catchment — Exploring  
805 sediment cascades using graph theory, 182, 89–103, <https://doi.org/10.1016/j.geomorph.2012.10.033>, 2013.
- Heckmann, T., Cavalli, M., Cerdan, O., Foerster, S., Javaux, M., Lode, E., Smetanová, A., Vericat, D., and Brardinoni, F.: Indices of sediment connectivity: opportunities, challenges and limitations, *Earth-Science Rev.*, 187, 77–108, <https://doi.org/10.1016/j.earscirev.2018.08.004>, 2018.
- Helming, K., Römken, M. J. M., and Prasad, S. N.: Surface Roughness Related Processes of Runoff and Soil Loss: A Flume  
810 Study, *Soil Sci. Soc. Am. J.*, 62, 243–250, <https://doi.org/10.2136/sssaj1998.03615995006200010031x>, 1998.
- Hino, M., Fujita, K., and Shutto, H.: A laboratory experiment on the role of grass for infiltration and runoff processes, *J. Hydrol.*, 90, 303–325, [https://doi.org/10.1016/0022-1694\(87\)90073-4](https://doi.org/10.1016/0022-1694(87)90073-4), 1987.
- Horton, R. E.: The role of infiltration in the hydrologic cycle, *Eos, Trans. Am. Geophys. Unioneophysical Union*, 14, 446–460, 1933.
- 815 Hudek, Sturrock, C. J., Atkinson, B. S., Stanchi, S., and Freppaz, M.: Root morphology and biomechanical characteristics of high altitude alpine plant species and their potential application in soil stabilization, *Ecol. Eng.*, 109, 228–239, <https://doi.org/10.1016/j.ecoleng.2017.05.048>, 2017.
- Ingle, J. C.: *The Movement of Beach Sand - An Analysis Using Fluorescent Grains*, 1st ed., Elsevier, [https://doi.org/10.1016/S0070-4571\(08\)X7030-X](https://doi.org/10.1016/S0070-4571(08)X7030-X), 1966.
- 820 Johnson, C. B., Mannering, J. V., and Moldenhauer, W. C.: Influence of Surface Roughness and Clod Size and Stability on Soil and Water Losses, *Soil Sci. Soc. Am. J.*, 43, 772–777, <https://doi.org/10.2136/sssaj1979.03615995004300040031x>, 1979.
- Jomaa, S., Barry, D. A., Heng, B. C. P., Brovelli, A., Sander, G. C., and Parlange, J.-Y.: Influence of rock fragment coverage on soil erosion and hydrological response: Laboratory flume experiments and modeling, *Water Resour. Res.*, 48, <https://doi.org/10.1029/2011WR011255>, 2012.
- 825 Jonasson, S. and Callaghan, T. V.: Root mechanical properties related to disturbed and stressed habitats in the Arctic, *New Phytol.*, 122, 179–186, <https://doi.org/10.1111/j.1469-8137.1992.tb00064.x>, 1992.
- Kato, S., Okabe, T., Aoki, Y., and Kamohara, S.: Field measurements of sand movement on river-mouth tidal flat using color sand tracing, *Coast. Eng. Proc.*, 1, 61, <https://doi.org/10.9753/icce.v34.sediment.61>, 2014.
- 830 Klaar, M. J., Kidd, C., Malone, E., Bartlett, R., Pinay, G., Chapin, F. S., and Milner, A.: Vegetation succession in deglaciated landscapes: implications for sediment and landscape stability, *Earth Surf. Process. Landforms*, 40, 1088–1100, <https://doi.org/10.1002/esp.3691>, 2015.
- Klein, M., Zviely, D., Kit, E., and Shteinman, B.: Sediment Transport along the Coast of Israel: Examination of Fluorescent

Sand Tracers, *J. Coast. Res.*, 236, 1462–1470, <https://doi.org/10.2112/05-0488.1>, 2007.

- 835 Knapen, A., Poesen, J., Govers, G., Gyssels, G., and Nachtergaele, J.: Resistance of soils to concentrated flow erosion: A review, *Earth-Science Rev.*, 80, 75–109, <https://doi.org/10.1016/j.earscirev.2006.08.001>, 2007.
- Komura, S.: Hydraulics of Slope Erosion by Overland Flow, *J. Hydraul. Div.*, 102, 1573–1586, <https://doi.org/10.1061/JYCEAJ.0004639>, 1976.
- Kuhn, M.: caret: Classification and Regression Training. R package version 6.0-90. <https://CRAN.R-project.org/package=caret>, 2021.
- 840 Labhart, T. P.: Aarmassiv und Gotthardmassiv, *Sammlung Geol. Führer*, 63, 173, 1977.
- Lane, S. N., Brookes, C. J., Kirkby, M. J., and Holden, J.: A network-index-based version of TOPMODEL for use with high-resolution digital topographic data, *Hydrol. Process.*, 18, 191–201, <https://doi.org/10.1002/hyp.5208>, 2004.
- Lane, S. N., Reaney, S. M., and Heathwaite, A. L.: Representation of landscape hydrological connectivity using a topographically driven surface flow index, *Water Resour. Res.*, 45, 1–10, <https://doi.org/10.1029/2008WR007336>, 2009.
- 845 Lavee, H. and Poesen, J. W. A.: Overland flow generation and continuity on stone-covered soil surfaces, *Hydrol. Process.*, 5, 345–360, <https://doi.org/10.1002/hyp.3360050403>, 1991.
- Lázaro, R., Calvo-Cases, A., Lázaro, A., and Molina, I.: Effective run-off flow length over biological soil crusts on silty loam soils in drylands, *Hydrol. Process.*, 29, 2534–2544, <https://doi.org/10.1002/hyp.10345>, 2015.
- 850 Leatherman, S. P.: Field Measurement of Microtopography, *J. Coast. Res.*, 3, 233–235, 1987.
- Legout, C., Leguédou, S., Le Bissonnais, Y., and Malam Issa, O.: Splash distance and size distributions for various soils, *Geoderma*, 124, 279–292, <https://doi.org/10.1016/j.geoderma.2004.05.006>, 2005.
- Li, D., Lu, X., Walling, D. E., Zhang, T., Steiner, J. F., Wasson, R. J., Harrison, S., Nepal, S., Nie, Y., Immerzeel, W. W., Shugar, D. H., Koppes, M., Lane, S., Zeng, Z., Sun, X., Yegorov, A., and Bolch, T.: High Mountain Asia hydropower systems threatened by climate-driven landscape instability, *Nat. Geosci.*, 15, 520–530, <https://doi.org/10.1038/s41561-022-00953-y>, 2022.
- 855 Lichtenegger, E.: Root distribution in some alpine plants, *Acta Phytogeogr. Suec.*, 81, 76–82, 1996.
- Lima, R. L. P. de, Abrantes, J. R. C. B., Lima, J. L. M. P. de, and Lima, M. I. P. de: Using thermal tracers to estimate flow velocities of shallow flows: laboratory and field experiments, *J. Hydrol. Hydromechanics*, 63, 255–262, <https://doi.org/10.1515/johh-2015-0028>, 2015.
- 860 Liu, Q. Q. and Singh, V. P.: Effect of Microtopography, Slope Length and Gradient, and Vegetative Cover on Overland Flow through Simulation, *J. Hydrol. Eng.*, 9, 375–382, [https://doi.org/10.1061/\(ASCE\)1084-0699\(2004\)9:5\(375\)](https://doi.org/10.1061/(ASCE)1084-0699(2004)9:5(375)), 2004.
- Lohse, K. A. and Dietrich, W. E.: Contrasting effects of soil development on hydrological properties and flow paths, *Water Resour. Res.*, 41, 1–17, <https://doi.org/10.1029/2004WR003403>, 2005.
- 865 Maier, F. and van Meerveld, I.: High-resolution soil surface photos of young moraines in the Swiss Alps. GFZ Data Services. <https://doi.org/10.5880/fidgeo.2023.016>, 2023.
- Maier, F. and van Meerveld, I.: Long-Term Changes in Runoff Generation Mechanisms for Two Proglacial Areas in the Swiss Alps I: Overland Flow, *Water Resour. Res.*, 57, 1–30, <https://doi.org/10.1029/2021wr030221>, 2021.
- 870 Maier, F., van Meerveld, I., Greinwald, K., Gebauer, T., Lustenberger, F., Hartmann, A., and Musso, A.: Effects of soil and vegetation development on surface hydrological properties of moraines in the Swiss Alps, 187, 104353, <https://doi.org/10.1016/j.catena.2019.104353>, 2020.
- Maier, F., van Meerveld, I., and Weiler, M.: Long-term changes in runoff generation mechanisms for two proglacial areas in the Swiss Alps II: Subsurface Flow, *Water Resour. Res.*, 2021.
- 875 Marchamalo, M., Hooke, J. M., and Sandercock, P. J.: Flow and Sediment Connectivity in Semi-arid Landscapes in SE Spain: Patterns and Controls, *L. Degrad. Dev.*, 27, 1032–1044, <https://doi.org/10.1002/ldr.2352>, 2016.

- Marques, M. J., Bienes, R., Jiménez, L., and Pérez-Rodríguez, R.: Effect of vegetal cover on runoff and soil erosion under light intensity events. Rainfall simulation over USLE plots, *Sci. Total Environ.*, 378, 161–165, <https://doi.org/10.1016/j.scitotenv.2007.01.043>, 2007.
- 880 Martínez-Carreras, N., Krein, A., Gallart, F., Iffly, J. F., Pfister, L., Hoffmann, L., and Owens, P. N.: Assessment of different colour parameters for discriminating potential suspended sediment sources and provenance: A multi-scale study in Luxembourg, 118, 118–129, <https://doi.org/10.1016/j.geomorph.2009.12.013>, 2010.
- Maruffi, L., Stucchi, L., Casale, F., and Bocchiola, D.: Soil erosion and sediment transport under climate change for Mera River, in Italian Alps of Valchiavenna, *Sci. Total Environ.*, 806, 150651, <https://doi.org/10.1016/j.scitotenv.2021.150651>, 2022.
- 885 Masselink, R. J. H., Heckmann, T., Temme, A. J. A. M., Anders, N. S., Gooren, H. P. A., and Keesstra, S. D.: A network theory approach for a better understanding of overland flow connectivity, *Hydrol. Process.*, 31, 207–220, <https://doi.org/10.1002/hyp.10993>, 2017.
- Medeiros, P. H. A. and de Araújo, J. C.: Temporal variability of rainfall in a semiarid environment in Brazil and its effect on sediment transport processes, *J. Soils Sediments*, 14, 1216–1223, <https://doi.org/10.1007/s11368-013-0809-9>, 2013.
- 890 MeteoSwiss. Swiss climate in detail. Extreme value analysis. Standard period 1990-2020. URL: <https://www.meteoschweiz.admin.ch/home/klima/schweizer-klima-im-detail/extremwertanalysen/standardperiode.html?station=grh> (last date accessed: 17.02.2022), 2021.
- MeteoSwiss. Swiss climate in detail. Climate diagrams and normals per station. Standard period 1991-2020. URL: <https://www.meteoschweiz.admin.ch/home/klima/schweizer-klima-im-detail/klima-normwerte/klimadiagramme-und-normwerte-pro-station.html?station=grh> (last date accessed: 17.02.2022), 2022.
- 895 Moreno-De Las Heras, M., Nicolau, J. M., Merino-Martín, L., and Wilcox, B. P.: Plot-scale effects on runoff and erosion along a slope degradation gradient, *Water Resour. Res.*, 46, 1–12, <https://doi.org/10.1029/2009WR007875>, 2010.
- Mu, H., Yu, X., Fu, S., Yu, B., Liu, Y., and Zhang, G.: Effect of stem basal cover on the sediment transport capacity of overland flows, *Geoderma*, 337, 384–393, <https://doi.org/10.1016/j.geoderma.2018.09.055>, 2019.
- 900 Musso, A., Lamorski, K., Sławiński, C., Geitner, C., Hunt, A., Greinwald, K., and Egli, M.: Evolution of soil pores and their characteristics in a siliceous and calcareous proglacial area, 182, 104–154, <https://doi.org/10.1016/j.catena.2019.104154>, 2019.
- Musso, A., Ketterer, M. E., Greinwald, K., Geitner, C., and Egli, M.: Rapid decrease of soil erosion rates with soil formation and vegetation development in periglacial areas, *Earth Surf. Process. Landforms*, 45, 2824–2839, <https://doi.org/10.1002/esp.4932>, 2020a.
- 905 Musso, A., Ketterer, M. E., Greinwald, K., Geitner, C., and Egli, M.: Rapid decrease of soil erosion rates with soil formation and vegetation development in periglacial areas, *Earth Surf. Process. Landforms*, 45, 2824–2839, <https://doi.org/10.1002/esp.4932>, 2020b.
- 910 Musso, A., Tikhomirov, D., Plötze, M.L., Greinwald, K., Hartmann, A., Geitner, C., Maier, F., Petibon, F. and Egli, M.: Soil formation and mass redistribution during the Holocene using meteoric <sup>10</sup>Be, soil chemistry and mineralogy. *Geosciences*, 12(2), p.99, <https://doi.org/10.3390/geosciences12020099>, 2022.
- Najafi, S., Dragovich, D., Heckmann, T., and Sadeghi, S. H.: Sediment connectivity concepts and approaches, 196, 104880, <https://doi.org/10.1016/j.catena.2020.104880>, 2021.
- 915 Nanda, A., Sen, S., and McNamara, J. P.: How spatiotemporal variation of soil moisture can explain hydrological connectivity of infiltration-excess dominated hillslope: Observations from lesser Himalayan landscape, *J. Hydrol.*, 579, 124146, <https://doi.org/10.1016/j.jhydrol.2019.124146>, 2019.
- Nearing, M. A., Pruski, F. ., and O’Neal, M. R.: Expected climate change impacts on soil erosion rates: A review, *J. Soil Water Conserv. Soc.*, 59, 43–50, 2004.

- 920 Noxton Technologies: Material safety data sheet of glow in the dark powder TAT 33, URL: [https://noxton.net/pasport\\_en.html](https://noxton.net/pasport_en.html), 2022.
- Orwin, J. F., Guggenmos, M. R., and Holland, P. G.: Changes in suspended sediment to solute yield ratios from an alpine basin during the transition to winter, southern alps, New Zealand, *Geogr. Ann. Ser. A Phys. Geogr.*, 92, 247–261, <https://doi.org/10.1111/j.1468-0459.2010.00393.x>, 2010.
- 925 Panagos, P., Borrelli, P., Poesen, J., Ballabio, C., Lugato, E., Meusburger, K., Montanarella, L., and Alewell, C.: The new assessment of soil loss by water erosion in Europe, *Environ. Sci. Policy*, 54, 438–447, <https://doi.org/10.1016/j.envsci.2015.08.012>, 2015.
- Park, S. W., Mitchell, J. K., and Bubenzer, G. D.: Rainfall Characteristics and Their Relation to Splash Erosion, *Trans. ASAE*, 26, 0795–0804, <https://doi.org/10.13031/2013.34026>, 1983.
- 930 Parsons, A. J.: *Overland Flow. Hydraulics and Erosion Mechanics.*, 1st ed., edited by: Parsons, A. J., CRC Press, London, 456 pp., <https://doi.org/10.1201/b12648>, 1992.
- Parsons, A. J.: Erosion and Sediment Transport by Water on Hillslopes, in: *Encyclopedia of Water*, Wiley, 1–10, <https://doi.org/10.1002/9781119300762.wsts0007>, 2019.
- Parsons, A. J., Onda, Y., Noguchi, T., Patin, J., Cooper, J., Wainwright, J., and Sakai, N.: The use of RFID in soil-erosion research, *Earth Surf. Process. Landforms*, 39, 1693–1696, <https://doi.org/10.1002/esp.3628>, 2014.
- 935 Paschmann, C., Fernandes, J. N., Vetsch, D. F., and Boes, R. M.: Assessment of flow field and sediment flux at alpine desanding facilities, *Int. J. River Basin Manag.*, 15, 287–295, <https://doi.org/10.1080/15715124.2017.1280814>, 2017.
- Pearce, R. A., Trlica, M. J., Leininger, W. C., Smith, J. L., and Frasier, G. W.: Efficiency of Grass Buffer Strips and Vegetation Height on Sediment Filtration in Laboratory Rainfall Simulations, *J. Environ. Qual.*, 26, 139–144, <https://doi.org/10.2134/jeq1997.00472425002600010021x>, 1997.
- 940 Peñuela, A., Darboux, F., Javaux, M., and Bièdiers, C. L.: Evolution of overland flow connectivity in bare agricultural plots, *Earth Surf. Process. Landforms*, 41, 1595–1613, <https://doi.org/10.1002/esp.3938>, 2016.
- Poesen, J.: Soil erosion in the Anthropocene: Research needs, *Earth Surf. Process. Landforms*, 84, 64–84, <https://doi.org/10.1002/esp.4250>, 2017.
- 945 Poesen, J. and Lavee, H.: Rock fragments in top soils: significance and processes, 23, 1–28, [https://doi.org/10.1016/0341-8162\(94\)90050-7](https://doi.org/10.1016/0341-8162(94)90050-7), 1994.
- Poesen, J., Ingelmo-Sanchez, F., and Mucher, H.: The hydrological response of soil surfaces to rainfall as affected by cover and position of rock fragments in the top layer, *Earth Surf. Process. Landforms*, 15, 653–671, <https://doi.org/10.1002/esp.3290150707>, 1990.
- 950 Pohl, M., Stroude, R., Buttler, A., and Rixen, C.: Functional traits and root morphology of alpine plants, *Ann. Bot.*, 108, 537–545, <https://doi.org/10.1093/aob/mcr169>, 2011.
- Pohlert, T.: *PMCMRplus: Calculate Pairwise Multiple Comparisons of Mean Rank Sums Extended*. R package version 1.9.4. <https://CRAN.R-project.org/package=PMCMRplus>, 2021.
- Polyakov, V., Li, L., and Nearing, M. A.: Correction factor for measuring mean overland flow velocities on stony surfaces under rainfall using dye tracer, *Geoderma*, 390, 114975, <https://doi.org/10.1016/j.geoderma.2021.114975>, 2021.
- 955 Polyakov, V. and Nearing, M. A.: Rare earth element oxides for tracing sediment movement, 55, 255–276, [https://doi.org/10.1016/S0341-8162\(03\)00159-0](https://doi.org/10.1016/S0341-8162(03)00159-0), 2004.
- R Core Team: A language and environment for statistical computing. R Foundation for Statistical Computing, Vienna, Austria. URL <https://www.R-project.org/>, 2021.
- 960 Reaney, S. M., Bracken, L. J., and Kirkby, M. J.: The importance of surface controls on overland flow connectivity in semi-arid environments: results from a numerical experimental approach, *Hydrol. Process.*, 28, 2116–2128, <https://doi.org/10.1002/hyp.9769>, 2014.

- Rey, F.: Influence of vegetation distribution on sediment yield in forested marly gullies, 50, 549–562, [https://doi.org/10.1016/S0341-8162\(02\)00121-2](https://doi.org/10.1016/S0341-8162(02)00121-2), 2003.
- 965 Rey, F., Ballais, J.-L., Marre, A., and Rovéra, G.: Role of vegetation in protection against surface hydric erosion, *Comptes Rendus Geosci.*, 336, 991–998, <https://doi.org/10.1016/j.crte.2004.03.012>, 2004.
- Richards, J. A.: Supervised Classification Techniques, in: *Remote Sensing Digital Image Analysis*, Springer Berlin Heidelberg, Berlin, Heidelberg, 247–318, [https://doi.org/10.1007/978-3-642-30062-2\\_8](https://doi.org/10.1007/978-3-642-30062-2_8), 2013.
- Schneider, P., Pool, S., Strouhal, L., and Seibert, J.: True colors – experimental identification of hydrological processes at a hillslope prone to slide, *Hydrol. Earth Syst. Sci.*, 18, 875–892, <https://doi.org/10.5194/hess-18-875-2014>, 2014.
- 970 Sen, S., Srivastava, P., Dane, J. H., Yoo, K. H., and Shaw, J. N.: Spatial-temporal variability and hydrologic connectivity of runoff generation areas in a North Alabama pasture-implications for phosphorus transport, *Hydrol. Process.*, 24, 342–356, <https://doi.org/10.1002/hyp.7502>, 2010.
- Shore, M., Murphy, P. N. C., Jordan, P., Mellander, P.-E., Kelly-Quinn, M., Cushen, M., Mechan, S., Shine, O., and Melland, A. R.: Evaluation of a surface hydrological connectivity index in agricultural catchments, *Environ. Model. Softw.*, 47, 7–15, <https://doi.org/10.1016/j.envsoft.2013.04.003>, 2013.
- 975 Sidle, R. C., Hirano, T., Gomi, T., and Tomomi, T.: Hortonian overland flow from Japanese forest plantations — an aberration, the real thing, or something in between?, *Hydrol. Process.*, 21, 3237–3247, <https://doi.org/10.1002/hyp>, 2007.
- Singer, M. and Walker, P.: Rainfall runoff in soil erosion with simulated rainfall, overland flow and cover, *Soil Res.*, 21, 109, <https://doi.org/10.1071/SR9830109>, 1983.
- 980 Smith, M. W., Bracken, L. J., and Cox, N. J.: Toward a dynamic representation of hydrological connectivity at the hillslope scale in semiarid areas, *Water Resour. Res.*, 46, 1–18, <https://doi.org/10.1029/2009WR008496>, 2010.
- Stewart, R. D., Liu, Z., Rupp, D. E., Higgins, C. W., and Selker, J. S.: A new instrument to measure plot-scale runoff, *Geosci. Instrumentation, Methods Data Syst.*, 4, 57–64, <https://doi.org/10.5194/gi-4-57-2015>, 2015.
- 985 Stock, J. and Dietrich, W. E.: Valley incision by debris flows: Evidence of a topographic signature, *Water Resour. Res.*, 39, <https://doi.org/10.1029/2001WR001057>, 2003.
- Tarboton, D. G.: A new method for the determination of flow directions and upslope areas in grid digital elevation models, *Water Resour. Res.*, 33, 309–319, <https://doi.org/10.1029/96WR03137>, 1997.
- Tauro, F., Grimaldi, S., Petroselli, A., and Porfiri, M.: Fluorescent particle tracers for surface flow measurements: A proof of concept in a natural stream, *Water Resour. Res.*, 48, <https://doi.org/10.1029/2011WR011610>, 2012a.
- 990 Tauro, F., Grimaldi, S., Petroselli, A., Rulli, M. C., and Porfiri, M.: Fluorescent particle tracers in surface hydrology: a proof of concept in a semi-natural hillslope, *Hydrol. Earth Syst. Sci.*, 16, 2973–2983, <https://doi.org/10.5194/hess-16-2973-2012>, 2012b.
- Tauro, F., Petroselli, A., Fiori, A., Romano, N., Rulli, M. C., Porfiri, M., Palladino, M., and Grimaldi, S.: Technical Note: Monitoring streamflow generation processes at Cape Fear, *Hydrol. Earth Syst. Sci. Discuss.*, 1–25, <https://doi.org/10.5194/hess-2016-501>, 2016.
- 995 Thompson, S. E., Katul, G. G., and Porporato, A.: Role of microtopography in rainfall-runoff partitioning: An analysis using idealized geometry, *Water Resour. Res.*, 46, 1–11, <https://doi.org/10.1029/2009WR008835>, 2010a.
- Thompson, S. E., Harman, C. J., Heine, P., and Katul, G. G.: Vegetation-infiltration relationships across climatic and soil type gradients, *J. Geophys. Res. Biogeosciences*, 115, n/a-n/a, <https://doi.org/10.1029/2009JG001134>, 2010b.
- 1000 Vigiak, O., van Dijk, S. J. E., van Loon, E. E., and Stroosnijder, L.: Matching hydrologic response to measured effective hydraulic conductivity, *Hydrol. Process.*, 20, 487–504, <https://doi.org/10.1002/hyp.5916>, 2006.
- Wainwright, J., Parsons, A. J., and Abrahams, A. D.: Plot-scale studies of vegetation, overland flow and erosion interactions: case studies from Arizona and New Mexico, *Hydrol. Process.*, 14, 2921–2943, [https://doi.org/10.1002/1099-1085\(200011/12\)14:16/17<2921::AID-HYP127>3.0.CO;2-7](https://doi.org/10.1002/1099-1085(200011/12)14:16/17<2921::AID-HYP127>3.0.CO;2-7), 2000.
- 1005

- Weiler, M.: Mechanisms controlling macropore flow during infiltration: dye tracer experiments and simulations, ETH Zurich, 12–19 pp., 2001.
- Weiler, M. and Flühler, H.: Inferring flow types from dye patterns in macroporous soils, *Geoderma*, 120, 137–153, <https://doi.org/10.1016/j.geoderma.2003.08.014>, 2004.
- 1010 Wickham, H: *ggplot2: Elegant Graphics for Data Analysis*. Springer-Verlag New York, 2016.
- Wolstenholme, J. M., Smith, M. W., Baird, A. J., and Sim, T. G.: A new approach for measuring surface hydrological connectivity, *Hydrol. Process.*, 34, 538–552, <https://doi.org/10.1002/hyp.13602>, 2020.
- Yasso, W. E.: Formulation and use of fluorescent tracer coatings in sediment transport studies, *Sedimentology*, 6, 287–301, <https://doi.org/10.1111/j.1365-3091.1966.tb01896.x>, 1966.
- 1015 Young, R. A. and Holt, R. F.: Tracing Soil Movement with Fluorescent Glass Particles, *Soil Sci. Soc. Am. J.*, 32, 600–602, <https://doi.org/10.2136/sssaj1968.03615995003200040050x>, 1968.
- Zanandrea, F., Michel, G. P., Kobiyama, M., Censi, G., and Abatti, B. H.: Spatial-temporal assessment of water and sediment connectivity through a modified connectivity index in a subtropical mountainous catchment, 204, 105380, <https://doi.org/10.1016/j.catena.2021.105380>, 2021.
- 1020 Zhang, B., Yang, Y., and Zepp, H.: Effect of vegetation restoration on soil and water erosion and nutrient losses of a severely eroded clayey Plinthudult in southeastern China, 57, 77–90, <https://doi.org/10.1016/j.catena.2003.07.001>, 2004.
- Zhang, X., Liu, B., Wang, J., Zhang, Z., Shi, K. and Wu, S.: Adobe photoshop quantification (PSQ) rather than point-counting: A rapid and precise method for quantifying rock textural data and porosities. *Computers & Geosciences*, 69, pp.62-71, <https://doi.org/10.1016/j.cageo.2014.04.003>, 2014.
- 1025 Zhang, D.: *rsq: R-Squared and Related Measures*. R package version 2.0. <https://CRAN.R-project.org/package=rsq>, 2020.
- Zimmermann, B.: Spatial and temporal variability of soil saturated hydraulic conductivity in gradients of disturbance, *J. Hydrol.*, 361, 78–95, <https://doi.org/10.1016/j.jhydrol.2008.07.027>, 2008.

Table 1: Overview of the main characteristics (elevation, slope, aspect, dominant species, vegetation cover, rock cover, sand content of the upper 10 cm of the soil, and the tortuosity index) for the five study plots.

Moraine	Plot name	Veg. complexity	Elevation (m a.s.l.)	Slope (°)	Aspect (°)	Dominant vegetation	Veg. cover (%)	Rock cover (%)	Sand content (%) <sup>1</sup>	Tortuosity index (-) <sup>2</sup>
1860	1860L	low	1989	28	49 NE	<i>Anthoxanthum alpinum</i> , <i>Salix retusa</i>	80	3	89	0.29
	1860M	medium	1981	36	56 NE	<i>Campanula scheuchzeri</i> , <i>Trifolium pallescens</i>	80	2	65	0.29
1990	1990L	low	1952	21	48 NE	<i>Salix hastata</i>	50	30	72	0.52
	1990M	medium	1959	29	56 NE	<i>Epilobium fleischeri</i> , <i>Poa alpina</i>	30	12	77	0.36
	1990H	high	1955	22	28 NE	<i>Salix retusa</i> , <i>Trifolium pallescens</i>	45	19	75	0.55

<sup>1</sup> from Hartmann et al. (2020b).

<sup>2</sup> calculated by the method of Bertuzzi et al. (1990), based on the normalized line length for ten measurements on each plot with a microtopography profiler of 1.5 m length (cf. Leatherman, 1987).



Table 2: Overview of the main response characteristics for all low, medium and high-intensity sprinkling experiments (LI, MI and HI, respectively) on all five plots.  $P_{tot}$  is the total rainfall amount,  $P_{int}$  is the average rainfall intensity,  $t_p$  is the rainfall duration,  $OF_{tot}$  is the total overland flow (OF),  $OF_{peak}$  is the peak OF rate,  $T_{peak}$  is the peak turbidity,  $S_y$  is the sediment yield,  $\Delta D$  is the percent change in sand distance, and  $\Delta A$  is the percent change in sand-covered area.

Moraine	Plot	Experiment	$P_{tot}$ (mm)	$P_{int}$ (mm hr <sup>-1</sup> )	$t_p$ (min)	$OF_{tot}$ (mm)	$OF_{peak}$ (mm h <sup>-1</sup> )	$T_{peak}$ (NTU)	$S_y$ (g)	$\Delta D$ (%)	$\Delta A$ (%)
1860	1860L	LI	23	20	69	0	0	0	0	-15	-16
		MI	25	43	35	1	4.9	11	1	31	-19
		HI	57	81	42	1.7	6.9	12	2	103	87
	1860M	LI	23	22	64	0	0	0	0	-46	-52
		MI	52	56	56	0	0	0	0	11	-27
		HI	63	90	42	1.3	7.2	2	0	-3	-38
1990	1990L	LI	19	15	75	1.4	0.5	48	1	253	272
		MI	30	37	48	3.1	8	83	28	334	198
		HI	32	48	40	3.6	10.6	134	46	265	211
	1990M	LI	21	23	55	0	0	0	0	152	139
		MI	33	54	37	0	0	0	0	190	165
		HI	36	61	35	2.4	9.2	39	4	175	160
	1990H	LI	18	14	75	1.9	2.4	7	0	15	22
		MI	27	33	49	1.6	3.3	89	6	38	24
		HI	27	46	35	1.8	5.4	94	15	79	26

1040

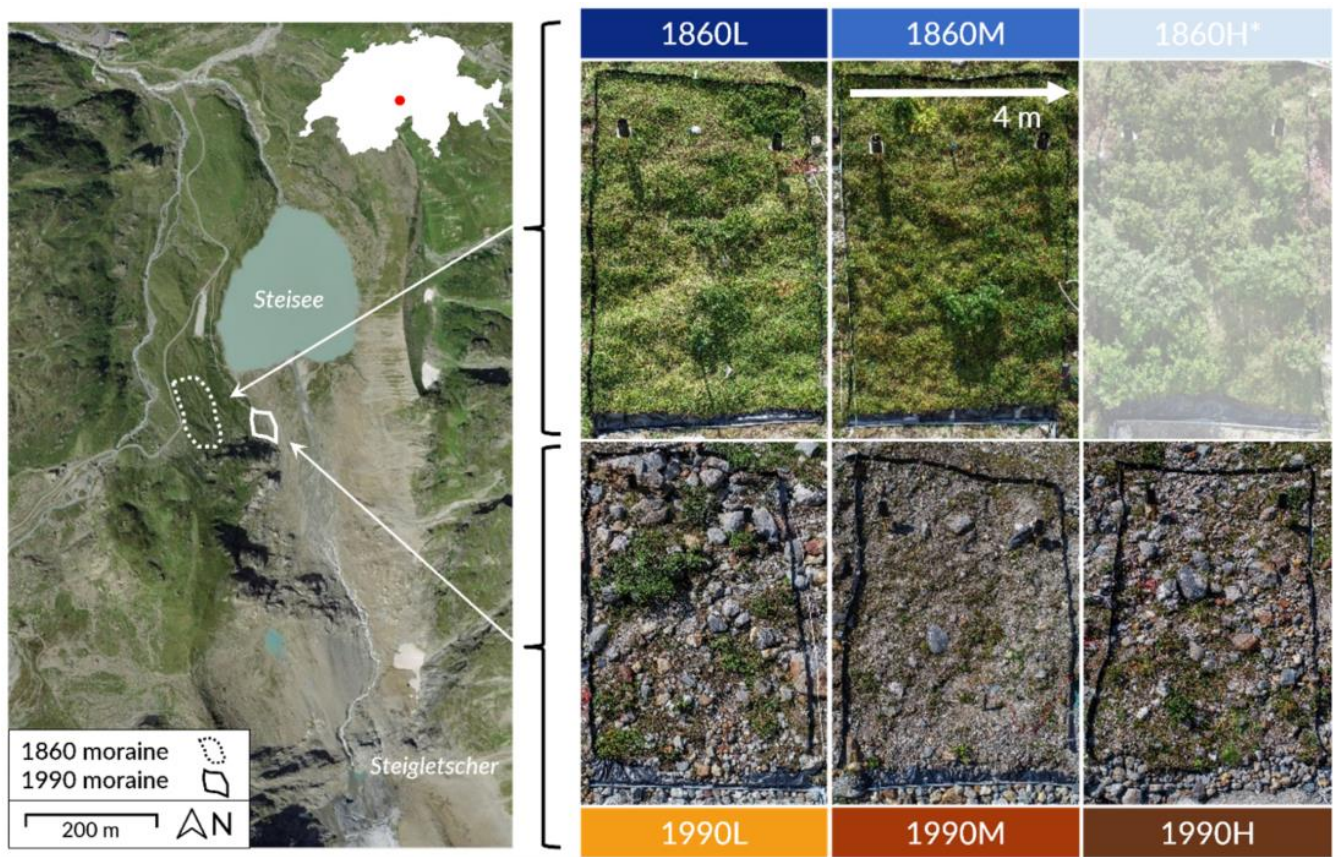
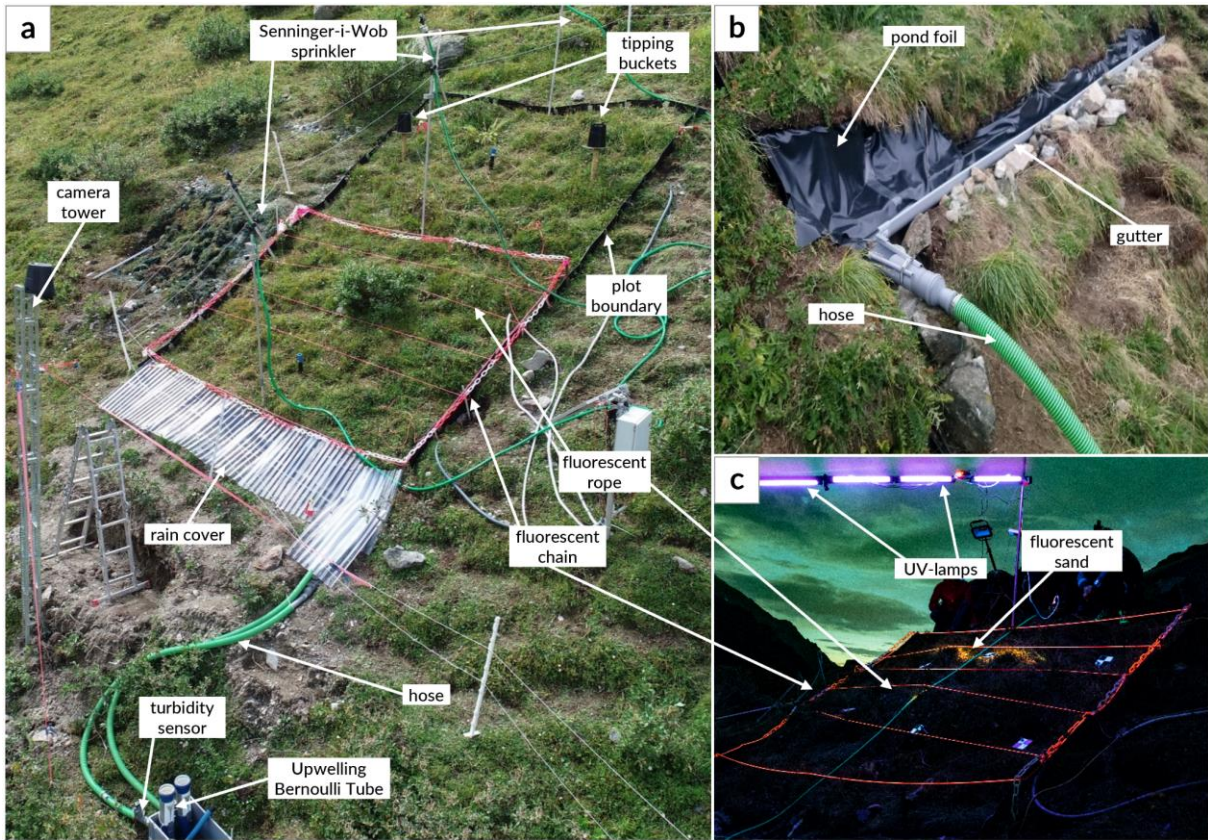


Figure 1: Aerial image of the Sustenpass study area (left) and photographs of the three experimental plots (right) on the 1860 and 1990 moraines. The outlines of the two studied moraines are indicated on the aerial image of the study area (1860 moraine: dashed line; 1990 moraine: solid line). The vegetation cover for the older (1860) moraine (top right) is much higher than for the younger (1990) moraine (bottom right). The 1860H plot was excluded from the analyses due to the dense shrub cover. Source of the aerial image: Federal Office of Topography Swisstopo ('Journey through time', 2019).

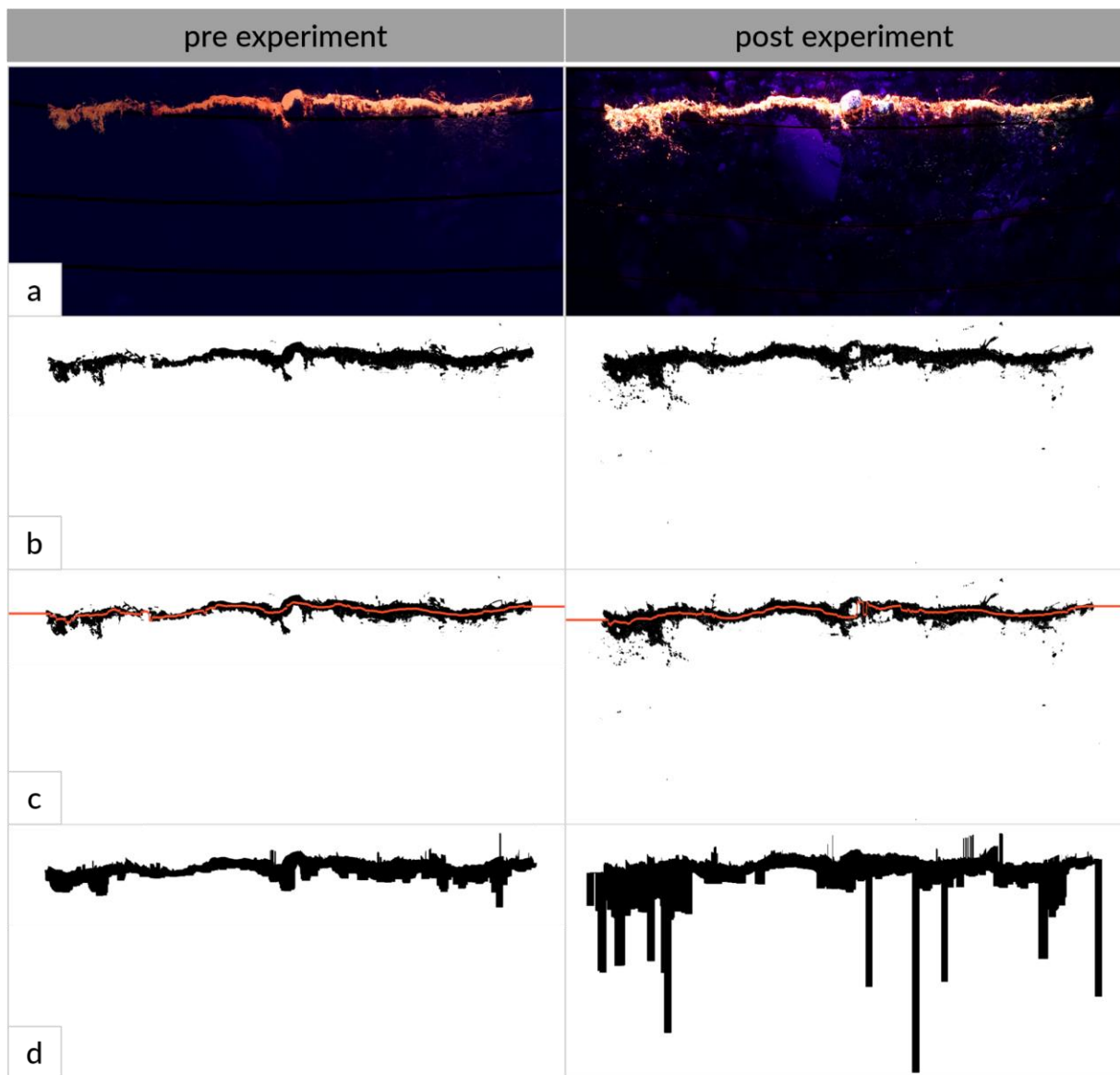
1045





1050

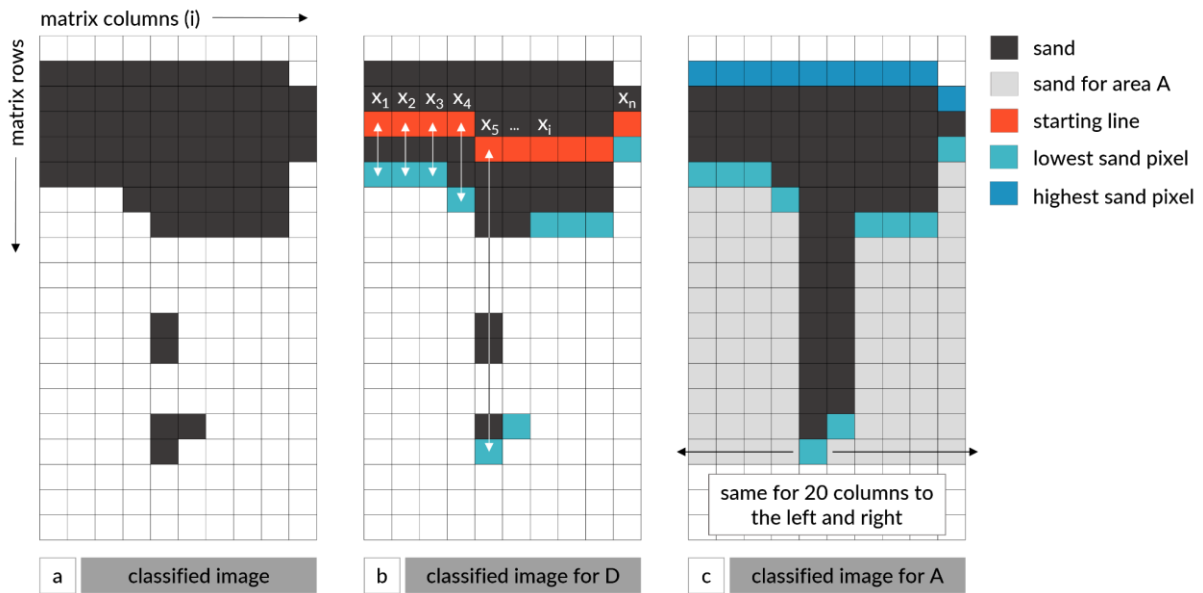
Figure 2: Photos showing the experimental set-up for the study plots (a), the collection system for overland flow, biomat and very shallow subsurface flow (OF) (b), and the set-up for the fluorescent sand imaging (c). Important components, such as the plot borders, sprinklers, tipping bucket rain gauges, pond foil, gutter and hose, turbidity sensor, Upwelling Bernoulli Tube, fluorescent segmented chain and fluorescent ropes, and camera tower below the plot are marked and labeled. At night UV lamps were used to illuminate the fluorescent sand on the plot (c).



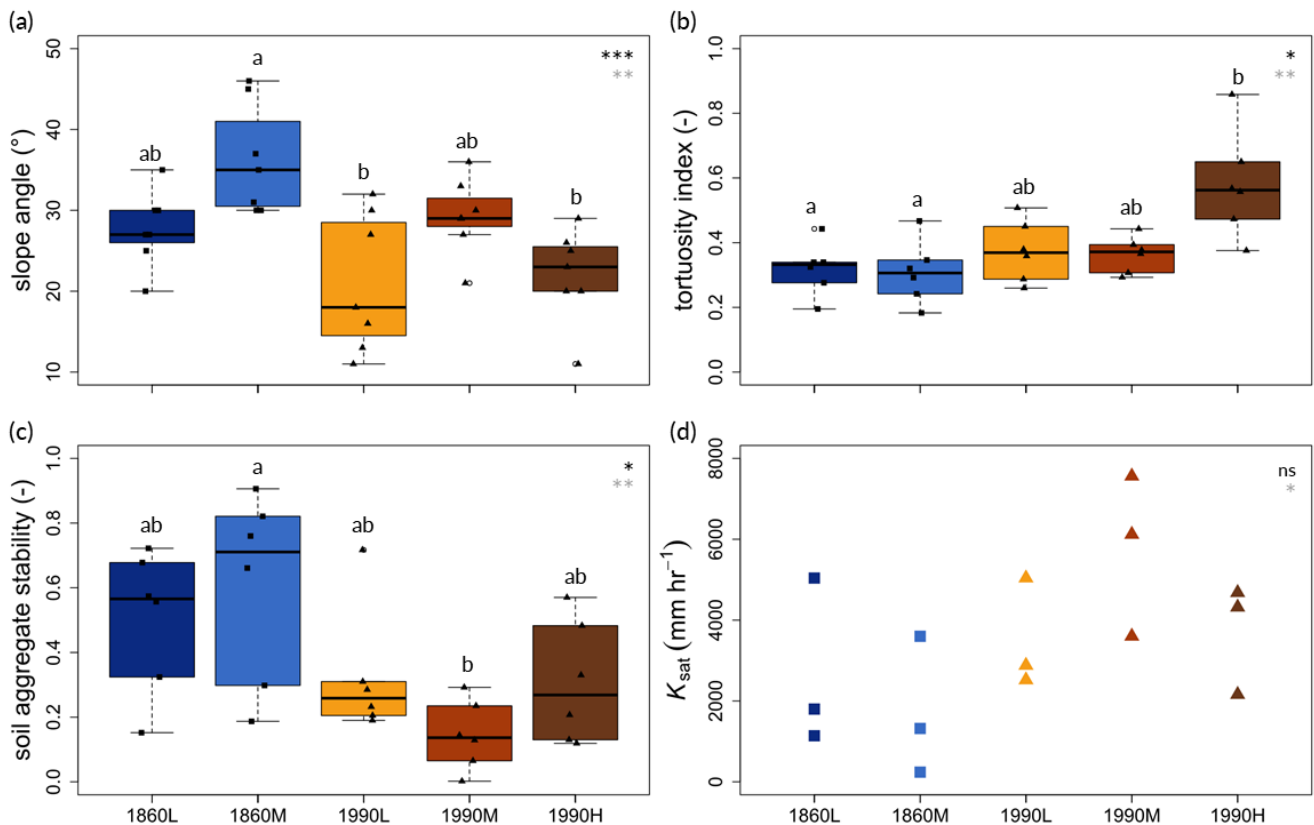
1055

Figure 3: Pre- and post-sprinkling experiments photographs (a) and visualization of the steps taken for the image analysis (b, c, d): geometrically corrected photos with the plot surroundings cut off and the fluorescent ropes digitally removed from the picture (a), classified images (a visual representation of a matrix containing zeros and ones), where classified pixels with fluorescent sand are shown in black (b), classified images with the location of the starting line (in red, at approximately the middle of the sand ribbon) for the determination of sand distances (c), and the calculated areas over which the sand was spread (d). The photos and images shown here are for the 1990M plot before and after the low intensity (LI) experiment. Please note that due to the downscaling of the photos and images not all sand particles are visible in the pictures shown in (a).

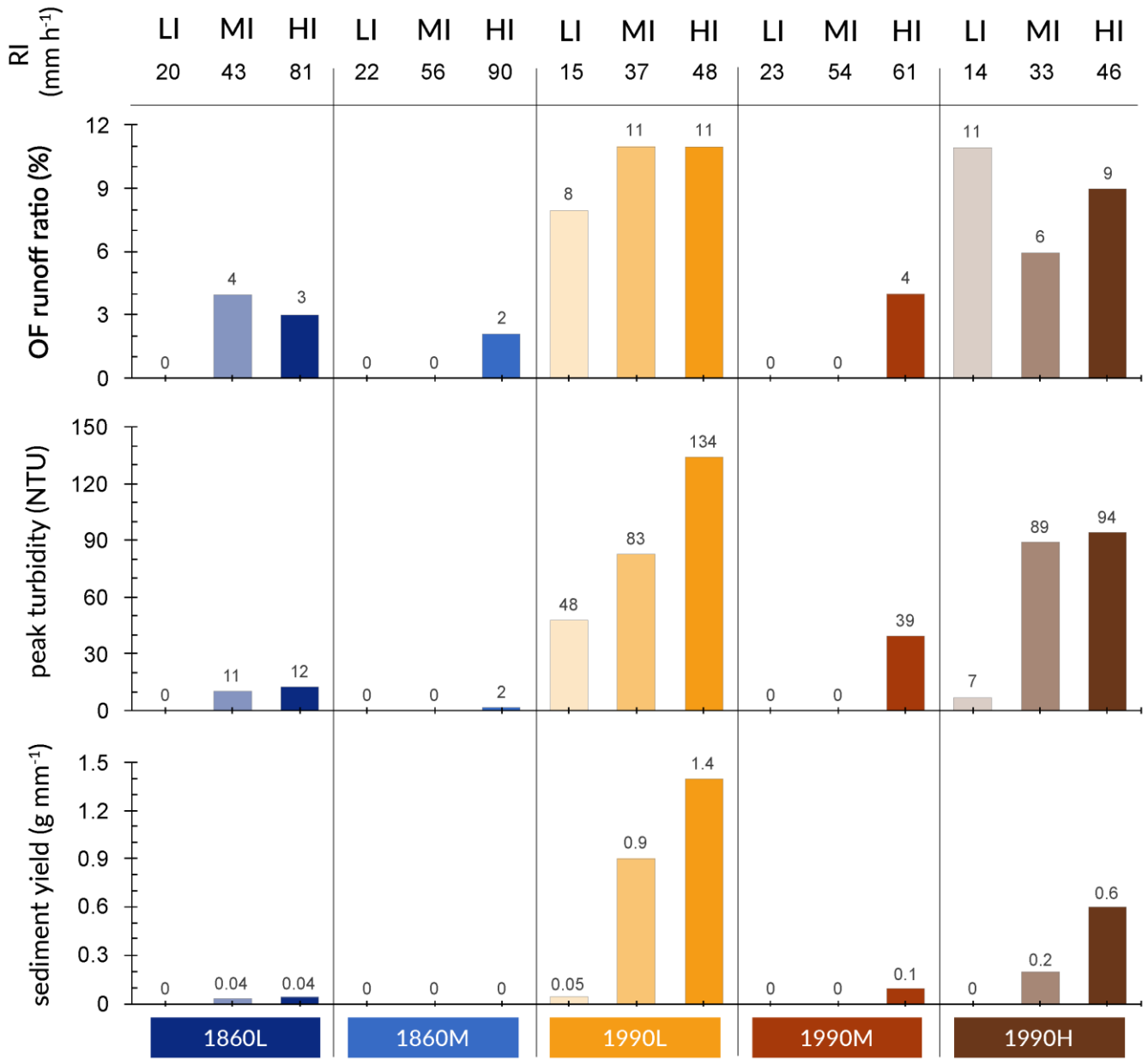
1060



1065 Figure 4: Sketch of the image analysis steps, showing a small part of a classified image where each square represents one  
 1070 pixel or element in the matrix (= 1 mm<sup>2</sup> on the plot). Pixels classified as sand are shown in black (a). For the determination  
 of the sand distance (D) in every column *i*, the distance ( $x_i$ ) between the starting line (red) and the lowermost sand pixel (shown  
 in turquoise) was determined (b). For the determination of the sand-covered area (A), all pixels between the uppermost (blue)  
 and lowermost sand pixel (turquoise) in each column and the 20 columns to the left and right were considered to be part of  
 area A (c).



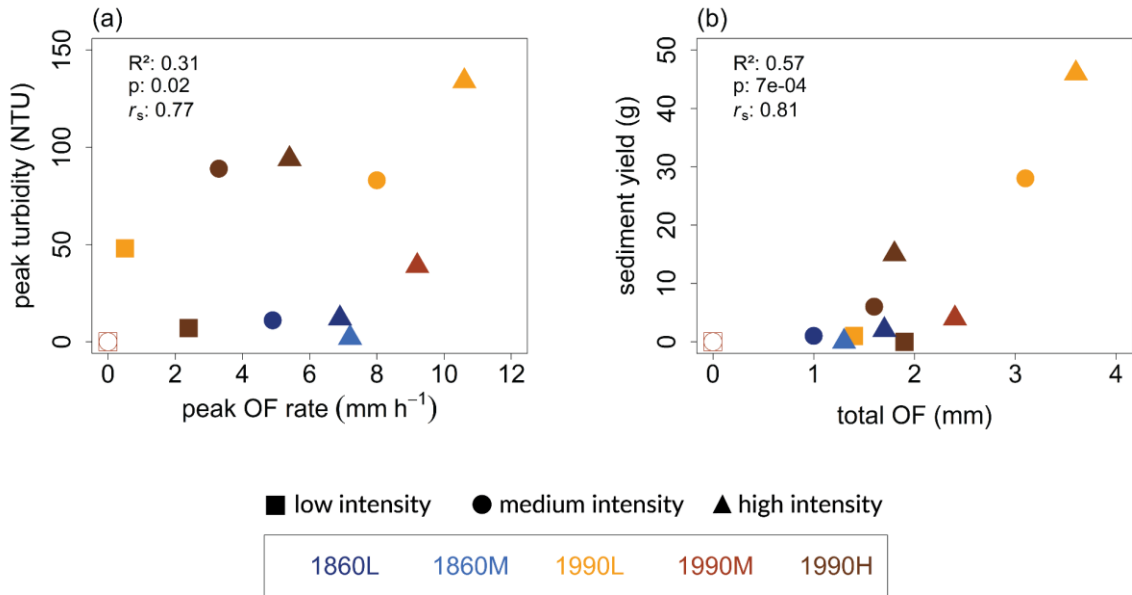
1075 Figure 5: Boxplots of the slope angle (a), tortuosity index (b), and aggregate stability of the top 10 cm of the soil (c), and the  
 saturated hydraulic conductivity ( $K_{sat}$ ) of the soil surface (d) for the five different plots. For the boxplots, the box represents  
 the 25<sup>th</sup> to 75<sup>th</sup> percentiles and the solid thick line the median. The whiskers extend to the 10<sup>th</sup> and 90<sup>th</sup> percentiles. The jittered  
 symbols represent the actual measurements (squares for the plots on the 1860 moraine and triangles for the plots on the 1990  
 moraine). The stars in the upper right corner of the plot indicate the level of significance for the differences in median values  
 for the five plots (top in black font), and between the two moraines (bottom in grey font): \* for  $p < 0.05$ , \*\* for  $p < 0.01$ , \*\*\*  
 for  $p < 0.001$ , and "ns" for  $p > 0.05$ . Plots that do not share a similar letter (shown above the boxplots) are statistically  
 significant different.



1080

Figure 6: Bar charts of the OF runoff ratio (%), peak turbidity (NTU), and the sediment yield per unit of precipitation ( $\text{g mm}^{-1}$ ) for each sprinkling experiment (LI, MI and HI represent low, mid and high intensity experiments, respectively) for each plot (1860L, 1860M, 1990L, 1990M, and 1990H). The absence of a bar indicates the lack of measurable OF (and thus also turbidity and sediment yield). OF and sediment yield were scaled by the amount of rainfall to improve the comparability for the different sprinkling experiments. The number above the bars denotes the value for each experiment. The number above the plot (RI = rainfall intensity) denotes the rainfall intensity (in  $\text{mm h}^{-1}$ ). The results for the unscaled values are similar and shown in the Supplementary Material (Figure S13).

1085



1090 Figure 7: Scatterplots showing the relation between the peak OF rate and peak turbidity (a) and between total overland flow  
 1095 and sediment yield (b) for all sprinkling experiments on the five plots (1860L, 1860M, 1990L, 1990M, and 1990H). The color  
 of the symbol represents the plot; the symbol represents the sprinkling experiment (low (LI), mid (MI), and high (HI) intensity).  
 The coefficient of determination (R<sup>2</sup>) and corresponding p-value, as well as the Spearman rank correlation coefficient (r<sub>s</sub>) are  
 given in the upper left corner of each subplot. Note that no OF was measured (and thus the peak OF rate, peak turbidity, and  
 total sediment yield were zero) for five of the 15 experiments, as indicated by the open symbols (note that only the result for  
 the 1990H LI and MI experiments are visible because the data points plot on top of each other).



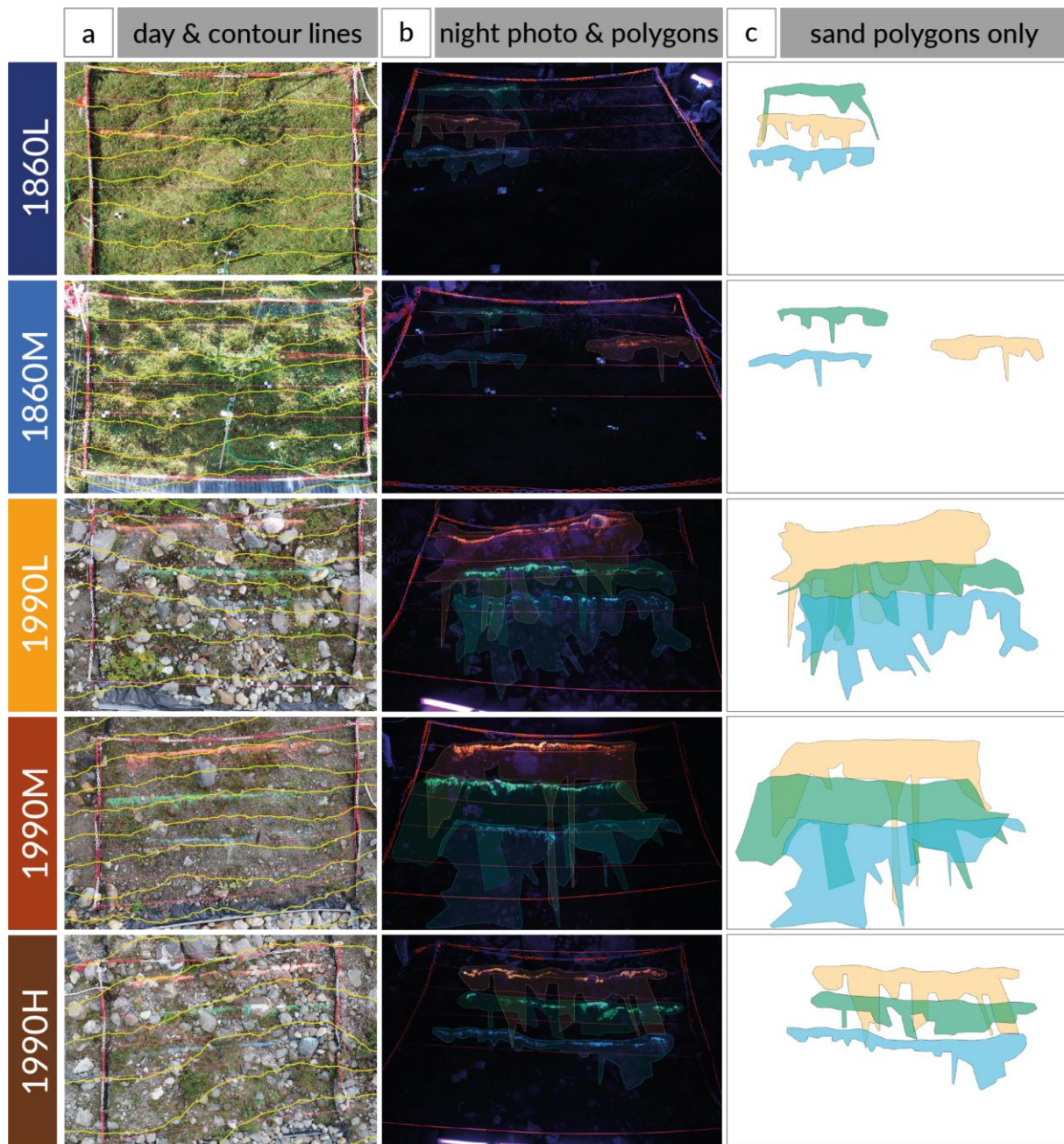
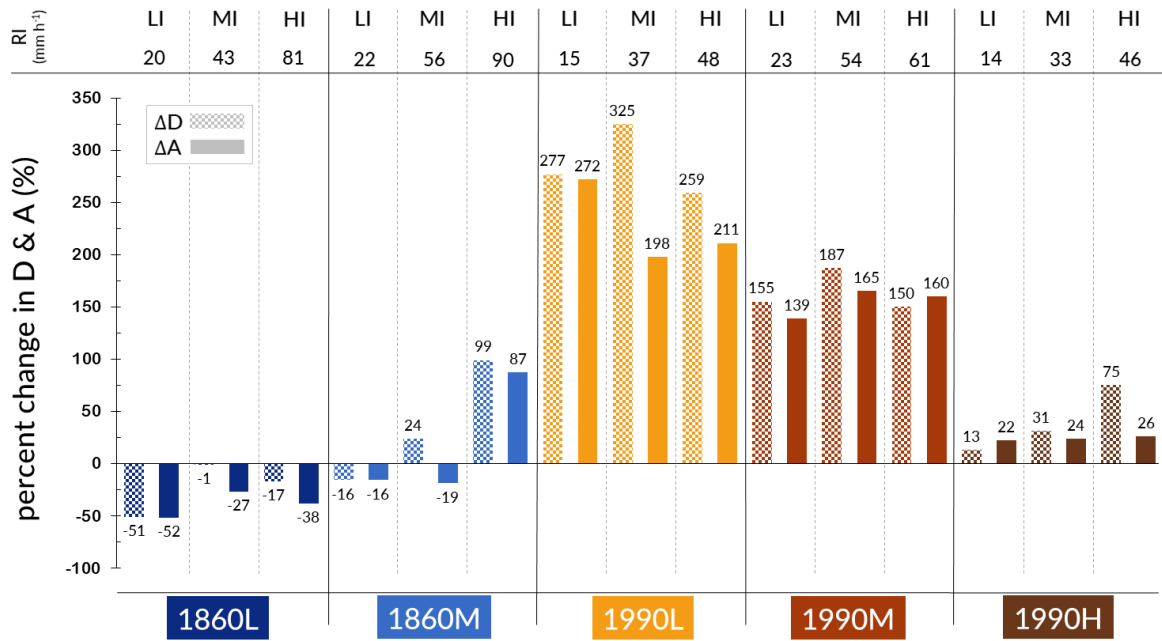


Figure 8: Photographs showing the sand-covered areas after the sprinkling experiments for the five plots. The left part (a) shows the daylight drone photos with the 50 cm contour lines (yellow lines). The orange sand ribbon was added prior to the low-intensity experiments (LI), the green sand prior to the medium intensity (MI) experiments, and the blue sand prior to the high intensity (HI) experiments. The central part (b) shows the nighttime photos taken after the experiments, while illuminating the fluorescent sand with the UV lamps. To better visualize the extent of the sand movement, hand-drawn polygons (translucent orange: LI experiment, green: MI experiment, and blue: HI experiment) depicting the maximum extent of the individual sand particles and clusters, were added to the photos. These polygons are also shown with a white background on the right side of the figure (c). The larger sand-covered areas (and transport distances) for the 1990 plots compared to the 1860 plots are reflected by the larger polygons. The full-size version of the daylight photos with the contour lines and the night photos of the fluorescent sand (without polygons) are given in the Supplementary Material (Figure S1 – S10) and are available in a higher resolution from Maier and van Meerveld (2023).

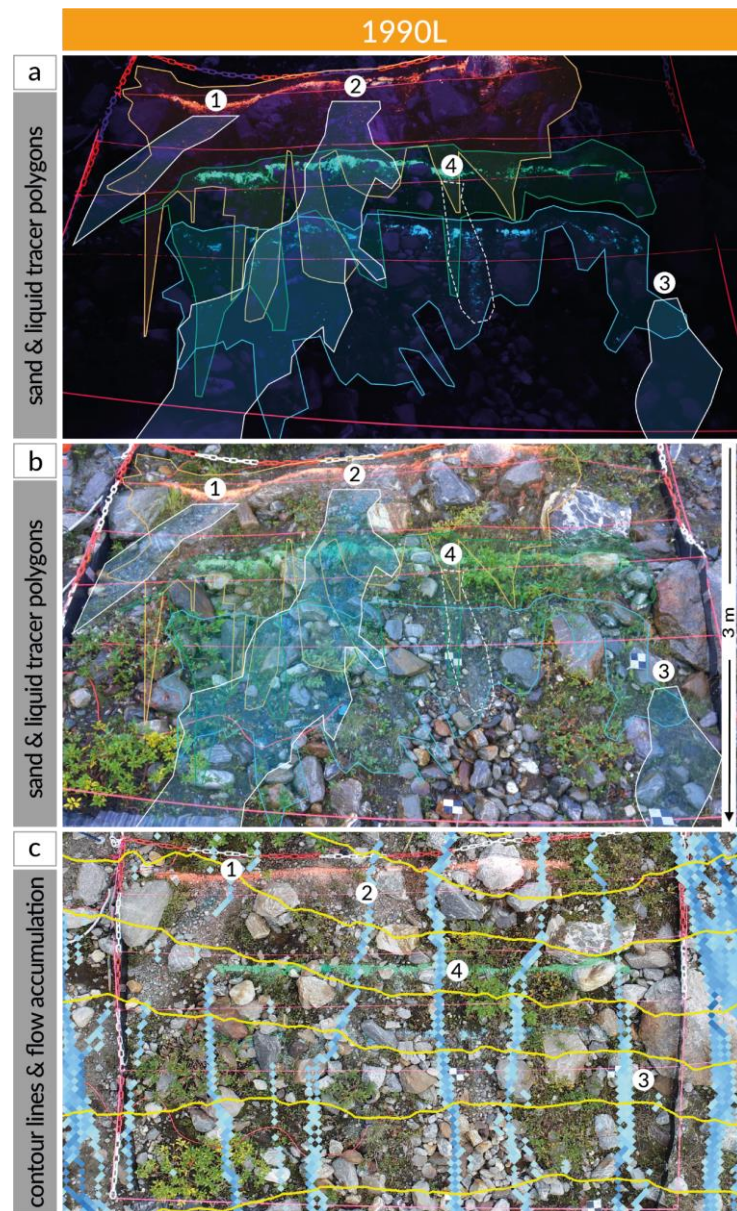




1110

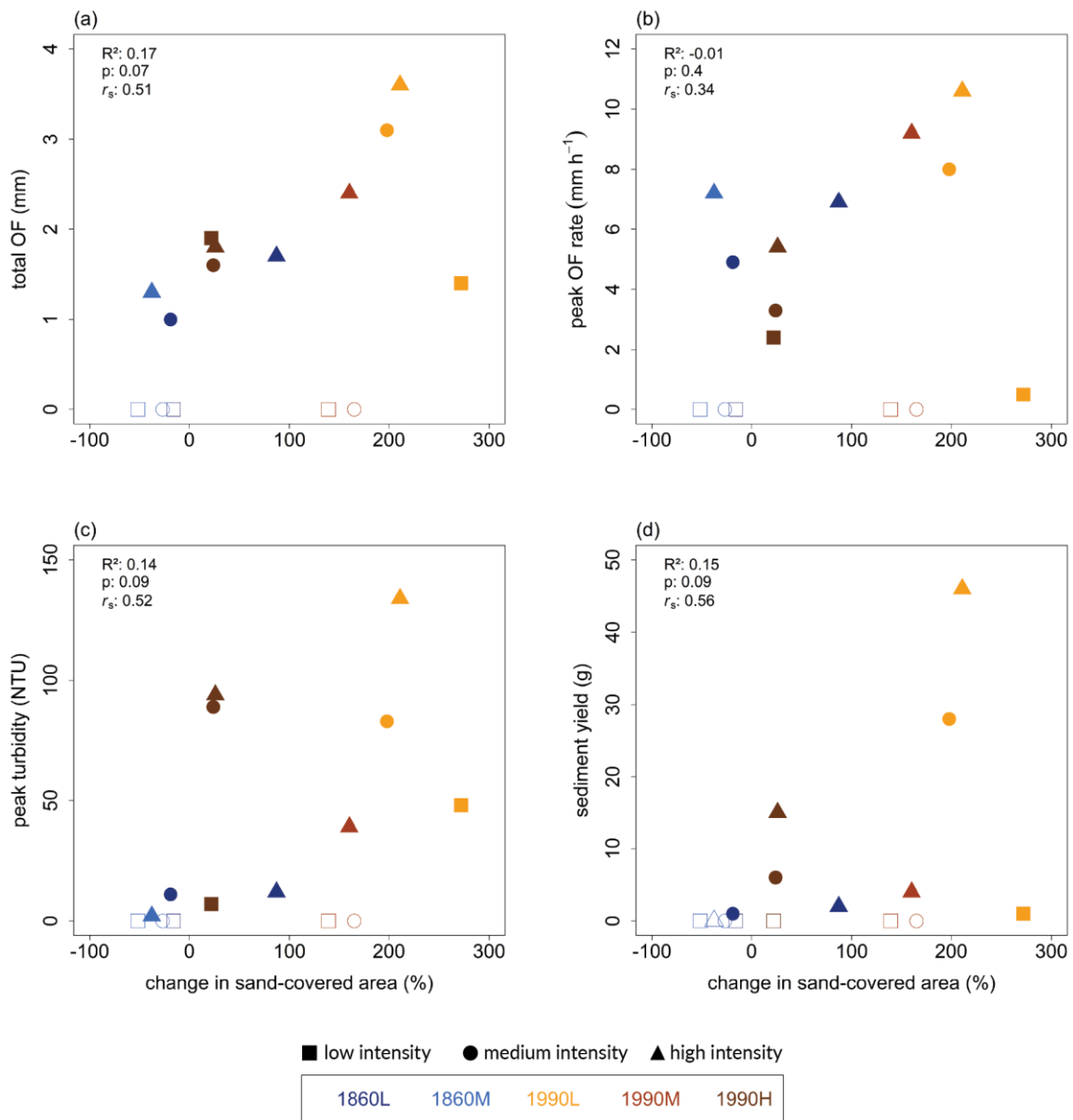
Figure 9: Change in the sand distance ( $\Delta D$ ; shaded bars) and sand-covered area ( $\Delta A$ ; solid bars) between the pre- and post-sprinkling conditions for all experiments on all five plots. LI, MI and HI represent low, medium and high-intensity sprinkling experiments. Positive changes reflect increases in sand distances and areas during the experiment and thus sand movement and deposition on the surface below the sand ribbon, while negative changes reflect a loss of sand from the surface (not an upward movement). The number above the plot (RI) denotes the rainfall intensity ( $\text{mm h}^{-1}$ ).

1115



1120

Figure 10: Overland flow (OF) pathways during the sprinkling experiments and sand-covered areas after the sprinkling experiments for the low complexity plot on the 1990 moraine (1990L). The upper photo (a) was taken at night and the hand-drawn orange, green and blue polygons (from Figure 8) were added to visualize the distribution of the fluorescent sand. The white polygons indicate OF pathways that were either clearly visible (#4) or traced by adding a brilliant blue tracer (#1, #2, #3) to the water during the sprinkling. Numbers 1 – 4 reflect specific flow pathways that are described in the text. The middle picture (b) is a composite of several video frames from the MI and HI experiments after the addition of the blue dye to visualize the OF pathways on the plot, again with the polygons that visualize the distribution of the fluorescent sand. The lower figure (c) shows a nadir view of the plot surface and includes the 50 cm contour lines (yellow) and the  $D_{\infty}$  derived flow accumulation (values larger than  $0.2 \text{ m}^2$  in blue).



1125

Figure 11: Scatterplots showing the relations between the change in sand-covered area ( $\Delta A$ ) and total overland flow (OF; a), peak OF rate (b), peak turbidity (c) and total sediment yield (d) for all sprinkling experiments. The color of the symbols represents the plots (1860L, 1860M, 1990L, 1990M, 1990H); the symbol represents the rainfall intensity of the sprinkling experiment (LI, MI, HI). Open symbols are used for experiments that did not generate any OF at the bottom of the plot (and consequently, for which there is no turbidity measurement or sediment yield). The coefficient of determination (R<sup>2</sup>) and corresponding p-value, as well as the Spearman rank correlation coefficient (r<sub>s</sub>), are given in the upper left corner of each subplot. The results for  $\Delta D$  are similar and shown in the Supplementary Material (Figure S11).

1130

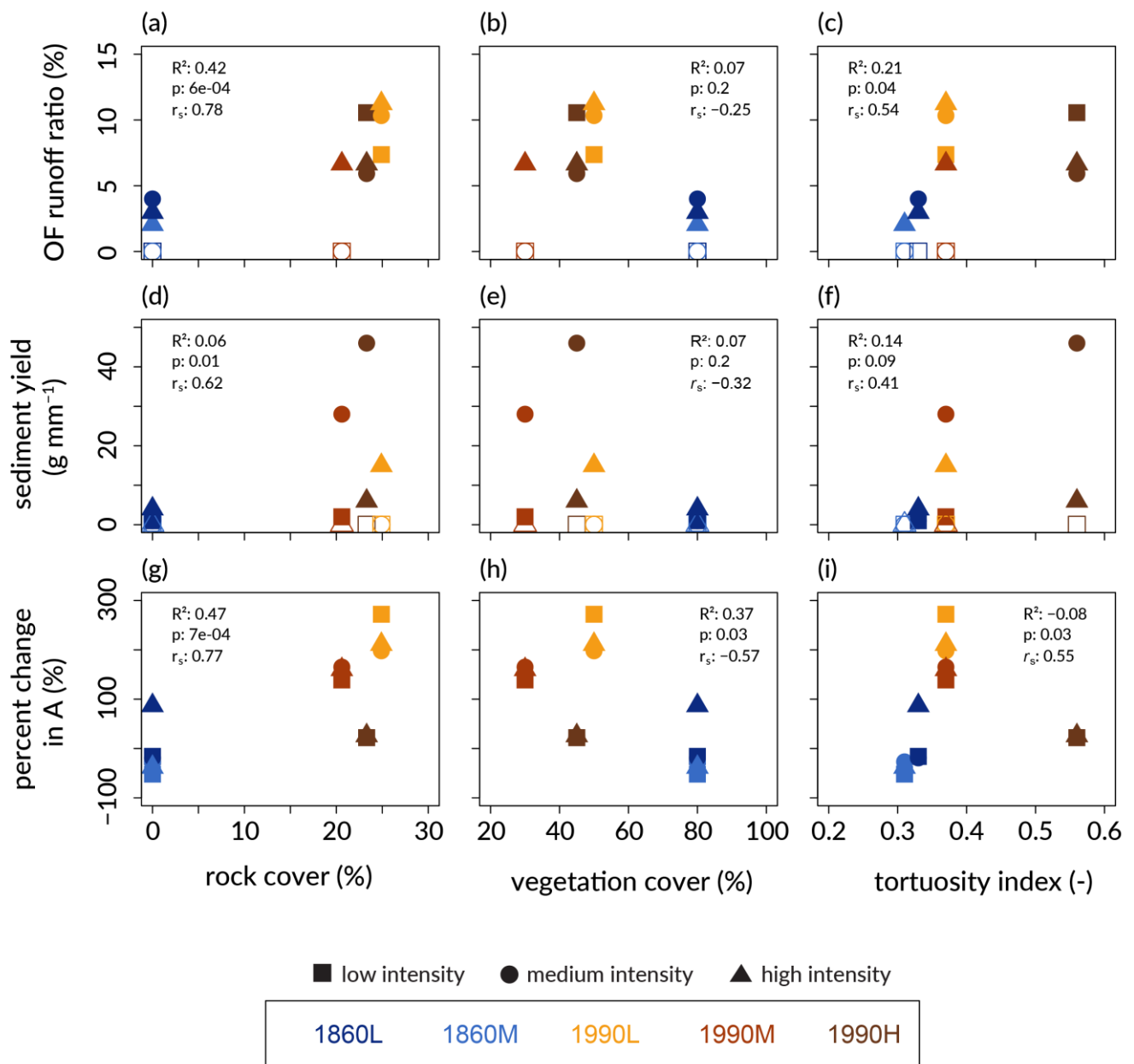


Figure 12: Scatterplots showing the relations between the OF runoff ratio (%), sediment yield per unit precipitation (g mm<sup>-1</sup>), percent change in sand-covered area ( $\Delta A$ ), and rock cover (%), vegetation cover (%), and tortuosity index (-) for all sprinkling experiments. The color of the symbols represents the plots (1860L, 1860M, 1990L, 1990M, 1990H); the symbol represents the rainfall intensity of the sprinkling experiment (LI, MI, HI). Open symbols are used for experiments that did not generate any OF at the bottom of the plot (and thus no sediment yield). The coefficient of determination (R<sup>2</sup>) and corresponding p-value, as well as the Spearman rank correlation coefficient (r<sub>s</sub>) are given in the upper left and right corner of each subplot.